

Ubiquity of human-induced changes in climate variability

Keith B. Rodgers^{1,2*}, Sun-Seon Lee^{1,2}, Nan Rosenbloom³, Axel Timmermann^{1,2,*}, Gokhan Danabasoglu³, Clara Deser³, Jim Edwards³, Ji-Eun Kim^{1,2}, Isla Simpson³, Karl Stein^{1,2}, Malte F. Stuecker⁴, Ryohei Yamaguchi^{1,2}, Tamas Bodai^{1,2}, Eui-Seok Chung⁵, Lei Huang^{1,2}, Who M. Kim³, Jean-François Lamarque³, Danica L. Lombardozzi³, William R. Wieder^{3,6}, Stephen G. Yeager³

1. Center for Climate Physics, Institute for Basic Science, Busan, South Korea
2. Pusan National University, Busan, South Korea
3. National Center for Atmospheric Research, Boulder, USA
4. Department of Oceanography and International Pacific Research Center, School of Ocean and Earth Science and Technology, University of Hawai'i at Mānoa, Honolulu, HI, USA
5. Korea Polar Research Institute, Incheon, South Korea
6. Institute of Arctic and Alpine Research, University of Colorado, Boulder, CO, USA

*Correspondence to: krodgers@pusan.ac.kr, axel@ibsclimate.org

While climate change mitigation targets necessarily concern maximum mean state changes, understanding impacts and developing adaptation strategies will be largely contingent on how climate variability responds to increasing anthropogenic perturbations. Here we present a new 100-member large ensemble of climate change projections conducted with the Community Earth System Model version 2 to examine the sensitivity of internal climate fluctuations to greenhouse warming. Our unprecedented simulations reveal that changes in variability, considered broadly in terms of probability distribution, amplitude, frequency, phasing, and patterns, are ubiquitous and span a wide range of physical and ecosystem variables across many spatial and temporal scales. Greenhouse warming will in particular alter variance spectra of Earth system variables that are characterized by non-Gaussian probability distributions, such as rainfall, primary production or fire occurrence. Our modeling results have important implications for climate adaptation efforts, resource management, and for seasonal predictions.

Teaser

Ubiquitous forced changes in natural variability are identified with a new Large Ensemble simulation.

40 MAIN TEXT

43 Introduction

44
45 Faced with the prospect of substantial future climate change, mitigation and adaptation
46 strategies are increasingly paramount. While mitigation efforts are concerned chiefly with
47 limiting mean state changes, successful adaptation will also require understanding the
48 potentially altered variability of the climate system (1). However, the way in which climate
49 variability will change as a result of anthropogenic radiative forcing has not been extensively
50 explored. The spectrum of observed regional-to-global climate fluctuations is characterized by
51 spectral variance peaks superimposed upon a broad noise background (2, 3). These peaks are
52 either caused by astronomical forcings or associated with spatio-temporal modes of internal
53 climate variability (4), such as the El Niño-Southern Oscillation (ENSO). How modes of
54 variability will respond to greenhouse warming has been addressed in a number of modeling
55 studies (5, 6), albeit with conflicting results. In contrast, the sensitivity of the spectral
56 background to human-induced climate change is less well-known. Identifying and
57 characterizing human-induced changes in this spectral background, using for example Climate
58 Model Intercomparison Project (CMIP)-type coordinated modeling efforts, has proven difficult
59 due to limited statistics.

60
61 The relatively recent advent of Large Ensemble simulations (henceforth termed Large
62 Ensembles) conducted with Earth system models provides a new resource for addressing how
63 climate and ecosystem statistics may evolve in response to anthropogenic greenhouse gas
64 forcing across a wide range of scales (7, 8). Such Large Ensembles with global climate models
65 have existed for more than 15 years (9-11), but earlier studies expressed concern with aspects
66 of process representation and therefore their results with regard to variability changes were
67 inconclusive. Other studies have employed individual model simulations, small (≤ 10 members)
68 ensembles, or CMIP multi-model ensembles (12-17) to address whether surface temperature
69 and precipitation variability may change under global warming. To date Large Ensemble studies
70 of changes in variance have mainly focused on specific quantities, timescales, or regions (7, 18-
71 21). However, to our knowledge, the full power of the Large Ensemble framework has not been
72 applied to gauge broad-scale forced changes in climate statistics, including changes in variance,
73 spectrum, pattern, phase and covariance, for a wide range of quantities, regions, and timescales.

74
75 To study the sensitivity of higher order climate statistics to anthropogenic climate
76 change, we conducted a new 100-member ensemble of climate change simulations using the
77 Community Earth System Model version 2 (CESM2) (22), which we refer to as CESM2-LE
78 (Methods). The initialization and forcing are described in Methods and figs. S1-S3 of the
79 Supplementary Materials. An ensemble of this size and duration with a CMIP6-generation Earth
80 system model at 1° spatial resolution is unprecedented. As such, it promises to provide an
81 enhanced framework for documenting and understanding robust forced changes in internal
82 variability, complementing our knowledge of mean-state changes (23, 24). The simulations
83 were performed for the 1850-2100 period with historical (1850-2014) and SSP3-7.0 (2015-
84 2100) forcings (see Methods for details on forcings and treatment of biomass burning, fig. S2),
85 and the choice of 100 members was motivated by the challenges associated with identifying
86 trends in higher-order statistical moments (25). To this end, substantial resources have been
87 devoted to providing high-frequency output for the atmosphere, land, ocean, and cryosphere

(see Data availability). Providing a clearer view of the patterns of altered climate variability should facilitate investigation of the mechanistic drivers of such changes and the implications for impacts of societal and ecosystem relevance. This study presents initial results on forced changes in internal variability across a range of quantities and timescales in CESM2-LE and will serve as the reference publication for CESM2-LE.

Results

Mean state changes

During the historical period the evolution of key simulated annual-mean climate indicators in CESM2-LE (**Fig. 1**; fig. S4) agrees well with observations. The range across the ensemble members, which results from internal variability and its forced changes, spans the observed climate state much of the time, with a notable exception of Southern Ocean sea-ice (**Fig. 1e**). The results here and the general model behavior are qualitatively consistent with those of similarly-forced CMIP6-generation models (24, 26, 27), although projected temperature changes (**Fig. 1c**) are in the upper range of the CMIP6 models owing to the relatively high climate sensitivity of CESM2 (28). The progressive weakening of the Atlantic Meridional Overturning Circulation (AMOC) in CESM2 over the 21st century (**Fig. 1f**) is largely consistent with other CMIP6 models (29). We also find a substantial increase in land primary production (**Fig. 1g**), which contributes to the uptake of carbon in the terrestrial biosphere. Marine net primary productivity (NPP) (**Fig. 1h**) remains relatively constant throughout the simulation and the overall uptake of carbon by the ocean reflects the re-emergence of anthropogenic carbon into the mixed layer (30, 31) and changes in the CO₂ buffering capacity of sea water (32).

The pattern of mean state surface temperature change, shown as the difference between the periods 2070-2099 and 1960-1989 (**Fig. 2**, central; 2m reference temperature shown in fig. S4), exhibits preferential warming of the eastern relative to the western equatorial Pacific, Arctic amplification, and a pronounced warming hole over the subpolar North Atlantic. These features are associated with the known mechanisms of the enhanced equatorial warming pattern (33), and more positive polar feedbacks (34) including the Arctic heat capacitor (35), and the slowdown of the AMOC (36, 37), respectively. For precipitation (**Fig. 2**, central; fig. S4e), changes include marked precipitation increases along the equatorial Pacific, within the Arctic Ocean, and decreases over the subtropical regions (38).

Forced changes in amplitude and frequency

Figure 2 illustrates the ensemble-aggregated Fourier amplitude spectra and probability density functions (PDFs) for five key climate and ecosystem quantities (complementary quantities are shown in fig. S5). For a wide range of Earth system variables, we find substantial changes of the projected 21st century probability distributions, impacting mean state, variance, and higher order statistical moments (**Fig. 2**). Human-induced alterations of climate probability distributions automatically translate into changes of the average return time of climate events. Averaging the spectra over 100 ensemble members and individual grid boxes within each region creates enough data to reveal spectral characteristics that might otherwise be obscured. The dominant feature for most quantities examined is the spectral peak at the annual frequency, along with higher-order harmonics that result from deviations of the seasonal cycle from a pure sinusoid. Future changes of the annual cycle overtone spectrum can be caused by forced non-

36 sinusoidal distortions of the annual cycle, generated e.g., by shifts in phenology, as discussed
37 below. For nearly all variables under consideration, the seasonal cycle amplitude responds to
38 the external forcing. Near-annual combination modes (C-modes) of ENSO and the seasonal
39 cycle (4) and its overtones can be clearly identified in some spectra, particularly for precipitation
40 over the equatorial Pacific. In addition to representing the C-modes as deterministic components
41 of the system, CESM2-LE also exhibits shifts in the frequency of the C-modes due to future
42 reductions in ENSO's dominant frequency (**Fig. 3a**). The C-mode peaks also strengthen in the
43 future, reflecting that the amplitude of precipitation and the corresponding C-mode-generating
44 nonlinearity increase at both ENSO and annual frequencies.

45
46 For most of the variables shown in **Fig. 2** (and fig. S5) there are changes in the amplitude
47 of the spectrum across the entire range of frequencies from decadal to interannual to intra-
48 seasonal to synoptic, revealing the ubiquity of variance changes. Importantly, frequency-
49 independent shifts in variance can be seen in the three variables shown here, which exhibit a
50 strong non-Gaussian skewed PDF, namely the spectra of California wildfire occurrence, surface
51 chlorophyll concentrations over the subpolar North Atlantic (40°N-60°N, 60°W-15°W), and
52 precipitation over the Niño3.4 region (5°S-5°N, 170°W-120°W). For these positive definite
53 variables, which are all characterized by a highly skewed probability distribution, forced
54 changes in the mean state are accompanied by a stretching (squeezing) of the associated PDFs,
55 thereby causing enhancement (or reduction) of variance and extremes. For stochastic processes,
56 the associated variance changes manifest as timescale-independent variance changes, thereby
57 accounting for the shown spectral background shifts. For California fire counts and Niño3.4
58 precipitation, mean state increases are therefore also accompanied by increases in variance
59 occurring over a wide range of timescales. For North Atlantic chlorophyll, the mean state
60 decrease is associated with a timescale-independent decrease in variance, with expected impacts
61 for higher trophic levels in the ocean, leading to potential disruptions of ecosystems.

62
63 For variables that are not positive-definite and less skewed, a diversity of responses is
64 found. Forced changes in sea surface temperature (SST) variability in the Niño3.4 region are
65 confined to interannual timescales in association with a decrease in ENSO amplitude and a
66 slight shift toward higher frequencies. On the other hand, for net ecosystem production (NEP)
67 over the Amazon, reflecting natural CO₂ exchange between the land and the atmosphere, there
68 is an increase in variance over all timescales, accompanied by a shift in the broad interannual
69 peak towards higher frequencies.

70
71 We next turn our attention to an expanded view of the temporal evolution of both
72 frequency and amplitude modulations of SST and precipitation over the Niño3.4 region
73 (170°W-120°W, 5°S-5°N) over the period 1960-2100. Ensemble Wavelet analysis of SST (**Fig.**
74 **3a**) and precipitation (**Fig. 3b**) within the Niño3.4 region has been conducted after first
75 removing the ensemble-mean trend over the full period from each ensemble member while
76 retaining the seasonal cycle. The wavelet analysis is conducted for each ensemble member and
77 then averaged. We consider the normalized variance to highlight the amplification above the
78 white noise level, and in contrast to **Fig. 2** represent variance with a linear scale to emphasize
79 temporal modulation of the amplitude of the maxima. For SST a clear separation is seen between
80 the maxima for interannual variability and the annual cycle (**Fig. 3a**). At interannual timescales,
81 there are two notable features. The first is a shift in the ENSO peak period from 3.5 years to
82 2.5 years between the end of the 20th and 21st centuries. The second feature with interannual

83 variability is that variance does not change monotonically, but rather exhibits a maximum
84 midway through the 21st century, similar to recent studies (39). This stands in contrast to
85 precipitation over the same region (**Fig. 3b**), for which there is a monotonic increase in variance,
86 following a similar shift in the period of the peak that was found for SST. For precipitation, the
87 amplitude of the seasonal cycle increases over 1960-2100, consistent with the notion of
88 precipitation variability enhancement over the tropics due to thermodynamic and dynamic
89 processes (40).

90
91 The forced changes over 1960-2100 in the structure of the seasonal cycle for the
92 ensemble-mean of SST (**Fig. 3c**), the ensemble-mean of precipitation (**Fig. 3d**), the standard
93 deviation (SD) of SST (**Fig. 3e**), and the SD of precipitation (**Fig. 3f**) are also considered for
94 the Niño3.4 region using daily-mean model output. The maximum (red dots) of ensemble-mean
95 SST occurs in May and the minimum (blue dots) in October in the late 20th century (**Fig. 3c**),
96 with both showing monotonic increases over 1960-2100. The maximum trends to two weeks
97 later and the minimum trends to two weeks earlier by the end of the 21st century, with this
98 modest perturbation to the phase of the seasonal cycle being accompanied by a modulation of
99 seasonal amplitude. The ensemble-mean seasonal maximum in precipitation (**Fig. 3d**) occurs
00 approximately one month before the ensemble-mean maximum in SST (**Fig. 3c**), and a second
01 maximum in precipitation in late January becomes evident during the second half of the 21st
02 century. On the other hand, the ensemble-mean minimum in precipitation occurs approximately
03 two weeks after the local minimum in temperature. The increase in the amplitude of the seasonal
04 cycle is thereby accompanied by changes in the phasing of the seasonal cycle for both SST and
05 precipitation.

06
07 The seasonally-stratified maximum cross-ensemble SD in SST (**Fig. 3e**), associated with
08 peak ENSO variability, exhibits a trend towards an earlier occurrence by approximately one
09 month over 1960-2070. This is accompanied by a modest decrease in amplitude (line plot). The
10 SD minimum for SST occurs in July for the 20th century, with a secondary minimum in the SD
11 developing over the first half of the 21st century in May. Subsequently the SD minimum in May
12 becomes more pronounced and becomes the dominant minimum in the SD of SST by the end
13 of the 21st century. For the SD of precipitation (**Fig. 3f**), there is a monotonic strengthening of
14 the seasonal maximum in late January, corresponding roughly to the time of peak ENSO
15 variability, and a weakening of the seasonal minimum in October, over the interval 1960-2100.
16 Whereas the seasonal minimum in the SD of precipitation (**Fig. 3f**) occurs nearly in phase with
17 the seasonal minimum of ensemble-mean SST (**Fig. 3c**), the seasonal maximum for the SD of
18 precipitation does not coincide with the seasonal maximum of ensemble-mean SST. Rather it
19 coincides with the secondary seasonal maximum in ensemble-mean precipitation in late January
20 (**Fig. 3d**).

21 22 23 **Changes in variance and covariance patterns**

24
25 Along with modulations in the frequency domain, the spatial patterns of variance are
26 altered in response to changing climate conditions. We begin by considering interannual
27 variance changes in boreal winter (December-January-February, DJF) by evaluating relative
28 changes in the cross-ensemble SD of surface temperature and precipitation for the same periods
29 as with the spectra in **Fig. 2** (1960-1989 and 2070-2099). The background cross-ensemble SD

30 averaged over 1960-1989 is shown in shading (**Fig. 4a,b**). Surface temperature (**Fig. 4a**) reveals
31 modest decreases in variability across the equatorial Pacific and Indian Oceans, consistent with
32 **Fig. 2**. Variability decreases over much of the higher latitudes of the Northern Hemisphere, with
33 exceptions over the Arctic and the North Atlantic, and with exceptions in the Southern
34 Hemisphere found over Southern Africa and parts of Antarctica (**Fig. 4a**). For precipitation (**Fig.**
35 **4b**) a relative increase in SD is seen over most regions with particularly pronounced
36 enhancements occurring in the eastern equatorial Pacific, the Indo-Pacific warm pool including
37 the South Pacific Convergence Zone, the western Arabian Sea, the poles, and most land areas.
38 The equatorial Pacific changes represent an eastward broadening in the centers of convection in
39 response to the enhanced equatorial Pacific warming and the reduction of the overall zonal SST
40 gradient (**Fig. 2, center**). In contrast, there is a decrease in the northern equatorial Atlantic
41 Ocean as well as in some trade wind regions of the eastern Pacific.

42
43 Another important question to address is whether greenhouse warming can also impact
44 the co-variability of different climate components and the global teleconnections of major
45 modes of climate variability. This is illustrated here by examining the projected changes in the
46 local correlation coefficients between the Niño3.4 SST index and surface temperature from
47 1960-1989 and 2070-2099 (**Fig. 4c**), with the background correlation coefficients shown in
48 shading and their respective future changes shown in circles. Our analysis reveals a systematic
49 strengthening of ENSO's remote temperature correlation over the Amazon basin and the
50 equatorial Atlantic, the Philippines and Japan in the western Pacific, throughout Africa, in
51 Northern India and across eastern Canada and the Southern US. Covariance decreases over
52 western Canada and Alaska, and zonally across the equatorial Indian Ocean.

53
54 The future changes in the correlation between the Niño3.4 index and precipitation (**Fig.**
55 **4d**) indicate a pattern of enhanced covariance over the western Pacific region surrounding the
56 Philippines, much of Africa and South America, and western China, as documented by the
57 background correlation coefficients and their future changes having the same sign. In other
58 words, in these regions we see stronger ENSO teleconnections under future global warming,
59 which in turn could translate to increased predictability of climate in these regions on seasonal
60 to interannual timescales, but also stronger impacts. In contrast, decreased precipitation
61 covariance with ENSO is found for North America over the Pacific Northwest as well as much
62 of the Southern U.S. and Mexico, as well as over Columbia/Venezuela, Bangladesh/Myanmar,
63 parts of eastern Australia, and parts of eastern Siberia. Taken together, the global pattern of
64 ENSO/precipitation covariance changes (**Fig. 4d**) is due to a combination of a simulated
65 weakening of ENSO SST variability (**Fig. 4a**) and eastward expansion of the region of
66 maximum convective activity in the equatorial Pacific (**Fig. 4b**) (analysis for the June-July-
67 August (JJA) season is shown in fig. S6), and likely other projected changes of the background
68 atmospheric circulation.

70 **Forced changes in phenology of net ecosystem productivity**

71
72 Finally, we illustrate how anthropogenic forcing impacts the phase of the seasonal cycle
73 by focusing on the phenology of NEP in the Northern Hemisphere mid-to-high latitudes (over
74 50°N-80°N). This is motivated by ecological concerns that a shift to an earlier spring bloom, in
75 particular over the land regions adjacent to the Arctic, can drive a phenological mismatch in
76 ecological interactions between plants and animals (41). Ensemble-mean NEP is integrated over

.77 this region in 5-year intervals (colors in **Fig. 5**, upper panel). We find an evolving amplitude of
.78 the seasonal cycle and of the growing season length (the interval during which NEP is positive,
.79 indicating net land uptake of carbon). This representation of forced changes in the non-
.80 sinusoidal seasonal cycle reveals that the growing season length is projected to increase by
.81 approximately three weeks, with the onset shifting two weeks earlier and termination shifting
.82 one week later. It also reveals a more than doubling of the amplitude of the seasonal cycle as a
.83 forced response. This represents an increase in the “breathing” of the terrestrial high latitude
.84 biosphere. Information from individual ensemble members in 20-year intervals regarding the
.85 timing of (i) first zero crossing, (ii) maximum NEP, (iii) second zero crossing, and (iv)
.86 maximum negative NEP (**Fig. 5**, lower panel) reveals that interannual variability is in general
.87 smaller than the forced trend evident in the ensemble mean in spring. This analysis indicates
.88 that for NEP aggregated over this region the phenological shift as a decadal trend becomes
.89 emergent relative to estimates of the natural variability already within the first decades of the
.90 21st century, a trend that is broadly consistent with observations (42, 43). Internal variability in
.91 the date of the onset of the growing season decreases by 36% over the course of the simulations
.92 and decreases by 18% for the date of the end of the growing season. The forced changes in
.93 growing season length are mostly attributable to changes in the mean temperature (44, 45). In
.94 contrast, the internal variability in the amplitude of the seasonal maximum increases by 63%
.95 over the simulations, and the absolute amplitude of the seasonal minimum increases by 22%
.96 over the course of the simulations.

.97 .98 .99 **Discussion** .00

.01 This study introduces a new, publicly available Large Ensemble of climate change
.02 simulations conducted with the global fully coupled CESM2 model (see Data availability). This
.03 Large Ensemble (CESM2-LE) is unprecedented in terms of size (100 members), duration (1850-
.04 2100), and spatial resolution in atmosphere and ocean (1°). As such, it affords a unique
.05 opportunity to study not only forced changes in the mean state, but also forced changes in
.06 internal variability, including higher-order statistical moments. Here we showcase aspects of
.07 the remarkable diversity of forced responses in amplitude, frequency, pattern, covariance, and
.08 seasonal characteristics of internal variability in CESM2-LE across a broad suite of key physical
.09 and ecosystem quantities, spanning the atmosphere, land, cryosphere, and ocean. Importantly,
.10 and contrary to conventional wisdom, the changes are not solely centered on the frequency of
.11 specific climate modes such as ENSO and the Madden Julian Oscillation, but are instead broadly
.12 distributed over nearly all timescales (**Fig. 2**), in particular for non-Gaussian distributed
.13 variables. The mechanistic underpinnings of the changes in variability go beyond amplification
.14 or damping of major climate modes, and possibly include state-dependence of linear stabilities,
.15 non-linearities, rectification, and changes in damping timescales and noise characteristics, many
.16 of which will be investigated in forthcoming studies analyzing the breadth of the CESM2-LE
.17 data.

.18
.19 If the ubiquitous changes in variance across temporal and spatial scales described here
.20 are realized in the real world, they will have a number of important implications for informing
.21 adaptation strategies and assessing potential impacts. This holds for water resource management
.22 and agriculture, fisheries, and occurrence of wildfires. Forced changes in phenology and phasing
.23 of the seasonal cycle for ecosystem productivity pose risks of mismatches with trophic level

24 interactions and energy transfers. The ubiquity of such changes in variability also points to the
25 importance of moving beyond the assumption of stationary variability in detection and
26 attribution studies of climate change (46), and underscores the necessity of recalibrating
27 climate-economy models (47) to account for an entirely different probability distribution for
28 variability (**Fig. 2**, fig. S5) than what is currently used when projecting future climate change
29 scenarios. The non-stationary nature of climate noise under anthropogenic forcing (**Fig. 2**) and
30 the evolving teleconnections patterns (**Fig. 4**) also have implications for seasonal to multi-year
31 climate predictability.

32

33 Although our analysis of the CESM2-LE has revealed a broad range of forced changes
34 in variance across physical scales and Earth system variables, it nevertheless should be
35 emphasized that model-uncertainty has not been considered here. There is already evidence for
36 the narrower case of interannual variability in surface temperature and precipitation that model
37 uncertainty in forced changes exhibits pronounced differences between models (21) (their
38 Supplementary Figures 7 and 8). Thus, it is our hope that our work will motivate further
39 investigations of forced changes in Earth system variance across a broad range of timescales
40 using existing archives of large ensemble simulations (7, 8).

41

42 Taken together, our analysis reveals an Earth system which is far more sensitive in its
43 statistical characteristics to greenhouse warming than previously recognized. Although only a
44 small fraction of such forced changes could be documented in this study, we expect that the
45 diagnostic ensemble analysis tools applied here, along with the open access to our datasets, will
46 inspire further investigations into the nonstationarity of Earth system processes in the presence
47 of anthropogenic forcing.

48

49

50

Materials and Methods

Experimental Design for Large Ensemble Simulations

The simulations consist of a 100-member large ensemble suite conducted with the Community Earth System Model Version 2 (CESM2) with the Community Atmosphere Model version 6 (CAM6)(22), namely the CESM2 LE. The simulations which cover the period from 1850-2100 follow SSP3-7.0 forcing protocols provided by the Coupled Model Intercomparison Project phase 6 (CMIP6) (48), although with some differences noted below for the representation of biomass burning in some of its ensemble members. The model has been demonstrated to fare well when evaluated against skill metrics against other models (24). The choice of the SSP3-7.0 scenario forcing follows CMIP6 recommendations (49) that emphasize the value of this “relatively high forcing level” precisely for the purpose of quantifying forced changes in natural variability. The choice of 100 members is motivated by our specific interest in evaluating variance changes in the Earth system, which places more stringent requirements on sufficient statistics for identifying changes(25).

The CESM2 components use nominal 1° horizontal resolution. Specifically, CAM6 has a resolution of 1.25° in longitude and 0.9° in latitude, and 32 vertical levels with a top at 2.26 hPa, or approximately 40km. The ocean and sea-ice models are the Parallel Ocean Program version 2 (POP2) (22, 50) and the CICE Version 5.1.2 (CICE5 (51)), and they share the same nominal 1° horizontal resolution. CESM2 offers a number of improvements pertinent to our scientific interests relative to early versions of CESM1 that motivated our choice of this model. A few of the important advances with the present model configuration relative to previous LE experiments include advances in the boundary layer representation for the ocean (52), as well as cloud microphysics (53). The ocean biogeochemistry model used within the POP2 model is the Marine Biogeochemistry Library (MARBL), which represents an updated version of what was previously known as the Biogeochemistry Elemental Cycle (54-56).

An important advance of great value to large ensemble investigations is through new developments incorporated into the Community Land Model Version 5 (CLM5) (22, 44, 45). This model has been demonstrated to address a number of well-known limitations including enhanced simulated cumulative CO₂ uptake over the historical period relative to previous versions of CLM (57). There have also been important improvements in the implementation of the prognostic fire model and the explicit representation of agricultural management (45, 58, 59). The improvements have been extensively documented through evaluation of model simulations against the International Land Model Benchmarking (60) (ILAMBv2.1) package (22, 44). In addition to the significant improvement to net ecosystem production (NEP) highlighted in our analysis of phenology changes in **Fig. 4**, improvements are found across a broad range of simulated variables in CLM5, relative to earlier versions of CLM.

Large Ensemble initialization

For the CESM2-LE initialization procedure, the experimental configuration was designed to respond to broad community requests for a mix of macro- and micro-perturbations (where for micro-perturbations members differ only in a small random perturbation applied at initialization). To satisfy this request and allow for exploration of the impact of initialization

type, it was decided to initialize members from various years between 1001 and 1301 of a pre-industrial simulation conducted with CESM2 (22), as this corresponds to a time when model drift is small, with the initialization procedure highlighted in fig. S1.

- i. Micro-initializations start from 4 different years: 1231, 1251, 1281, and 1301. 20 members were run for each start year, with ensemble spread introduced by a random perturbation to the temperature field at initialization (commonly referred to as “pertlim”), as was used for all members in the CESM1 large ensemble (61).
- ii. Macro-initiation (one run for each initialization date) using initialization years 1001, 1011, 1021, 1031, 1041, 1051, 1061, 1071, 1081, 1091, 1101, 1111, 1121, 1131, 1141, 1151, 1161, 1171, 1181, 1191, i.e., utilizing 20 independent restart files at 10-year intervals over 1001-1191. Note that for this case no explicit perturbation was required from the pre-industrial control simulation. Taken together, if one includes one member from each of the micro-perturbation runs, then a total of 24 macro-perturbation runs are available.

Importantly, as can be seen in fig. S1b, for the initiation points of years 1231, 1251, 1281, and 1301 were specifically chosen for the micro-initializations to correspond to years of maximum, decreasing, minimum, and increasing AMOC transport, respectively, relative to the preindustrial control simulation. For the analysis presented in the main text and figures, where the emphasis was on the two periods 1960-1989 and 2070-2099, we have assumed that the memory of the climate system of differences in the initial conditions from the control run (black lines in fig. S1) is no longer contributing to differences between ensemble members by 1950. Further quantitative exploration of the specific duration over which initial condition memory is retained is the subject of a separate ongoing study.

The macro-perturbation runs initialized in 1011, 1031, 1051, 1071, 1091, 1111, 1131, 1151, 1171, and 1191 have greatly enhanced output at high frequency to meet the needs of broader community interests for large ensemble output. This includes 6-hourly snapshots of three-dimensional temperature, winds, and specific humidity for the Coordinated Regional Climate Downscaling Experiment (<https://cordex.org>) simulations.

Forcings

A choice was made to use two different sets of forcing fields to represent the effects of variability in biomass burning emissions for the CESM2-LE (see figs. S2-S3). The biomass burning aerosol fluxes are imposed at the surface. As such, they are not prognostic, meaning that they are not generated by the model’s internal prognostic fire model. The first 50 members of our Large Ensemble follow CMIP6 protocols (62), with biomass burning following the description in the CESM2 overview paper (22). For the second set of 50 members, the CMIP6 biomass burning emissions of all relevant species for CAM6 were smoothed in time through an 11-year running mean filter. The averaging impacted variability in biomass burning fluxes over 1990-2020. The temporal smoothing of the forcing is applied to the biomass burning emissions at each gridpoint subsequent to being regridded to the CESM2 grid. The high 1990-2020 CMIP6 biomass burning variability (ensemble members 1-50) relative to the smoothed forcing (ensemble members 51-100) has a discernable impact on large-scale climate, as documented by the accelerated loss of September Arctic sea ice and northern hemispheric and tropical Pacific warming (fig. S3a,c).

Statistical Analysis

.45
.46
.47
.48
.49
.50
.51
.52
.53
.54
.55
.56
.57
.58
.59
.60
.61
.62
.63

For the wavelet power spectra in **Fig. 3a,b**, we used a Morlet wavelet, normalized by $\bar{\sigma}^{-2}$, where $\bar{\sigma}$ is the ensemble mean standard deviation of the respective Niño3.4 time series (63). An adjusted Welch's t -test was applied in **Fig. 4a,b**, as well as fig S4 and fig. S6a,b. The general approach is to first calculate the equivalent sample size \hat{n} , to account for potential serial correlation of the time series, which is then used to calculate the degrees of freedom of the Welch's t -test, which is an adjusted version of the Student's t -test that allows for the two samples to have unequal variance (i.e., heteroskedasticity). First, the decorrelation timescale T_e was calculated at each grid point, and for each period, based on the e-folding timescale of the autocorrelation function $r(\tau)$, defined as the smallest lag τ for which $r(\tau) < e^{-1}$. Then the equivalent sample size \hat{n} was defined as $\hat{n} = \frac{N}{T_e}$, where $N = 30$ is the total sample size in our case. The equivalent sample size was then used to calculate the degrees of freedom of the standard Welch's t -test. Note that this test may still be liberal if the equivalent sample sizes are small, i.e., in areas of high serial correlation.

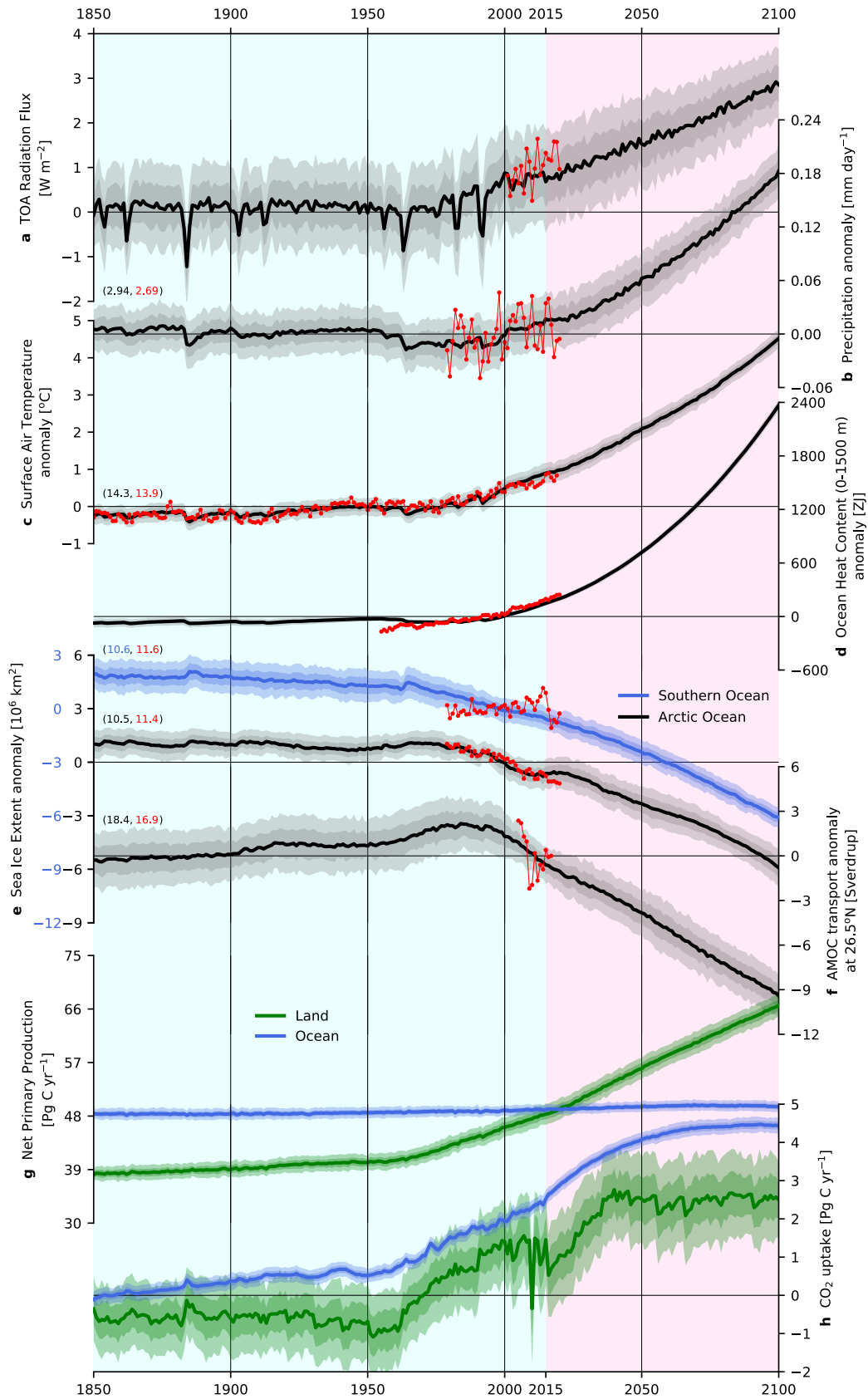


Fig. 1. Annual mean evolution of global fields over 1850-2100 for 100 members. For model fields, bold lines represent ensemble means, and dark and light shading represent one standard deviation (SD) and two SD variability. Observational data are shown in red when appropriate. Portions of the figure with light-blue background shading indicate

65
66
67
68
69
70

.71 the historical period (1850-2014) while portions with light-red background shading
.72 indicate the projection period (2015-2100). (a) Top of atmosphere radiative balance (W
.73 m^{-2}), along with the CERES-EBAF product (64), (b) anomalies of the global mean
.74 precipitation ($mm\ day^{-1}$), increasing 5.4% between the 1850s and the 2090s, compared
.75 with the Global Precipitation Climatology Project (GPCP) (65, 66), (c) anomalies of
.76 global mean surface temperature, increasing by 4.4°C between the 1850s and the 2090s,
.77 along with HadCRUT4 (67) anomalies over 1950-2019, (d) anomalies of ocean heat
.78 content integrated over the upper 1500m, along with an observation-based product (68),
.79 (e) anomalies of sea ice extent for the Arctic (black) and Southern Ocean (blue), with
.80 observed sea ice extent over 1979-2020 (69), and with the scales of the anomaly plots
.81 offset to facilitate comparison, (f) Atlantic Meridional Overturning Circulation
.82 (AMOC) transport anomalies at 26.5°N, with RAPID array observations (70), (g)
.83 globally-integrated net primary productivity (NPP) over the ocean (blue; increase of
.84 2.7% between the 1850s and the 2090s) and land (green; increase of 71% between the
.85 1850s and the 2090s), and globally-integrated net CO₂ fluxes over the ocean (solid blue)
.86 and integrated net CO₂ flux (net biome production, or NBP, including fire and land-use
.87 change) over land (green) with all quantities in (g) in units of $PgC\ yr^{-1}$. For each case,
.88 where observational products are included, anomalies are calculated with respect to the
.89 period spanned by the observations. For anomaly fields, printed numbers represent the
.90 absolute mean of the ensemble mean of CESM2-LE (black or blue numbers) and the
.91 observational product (red numbers).
.92

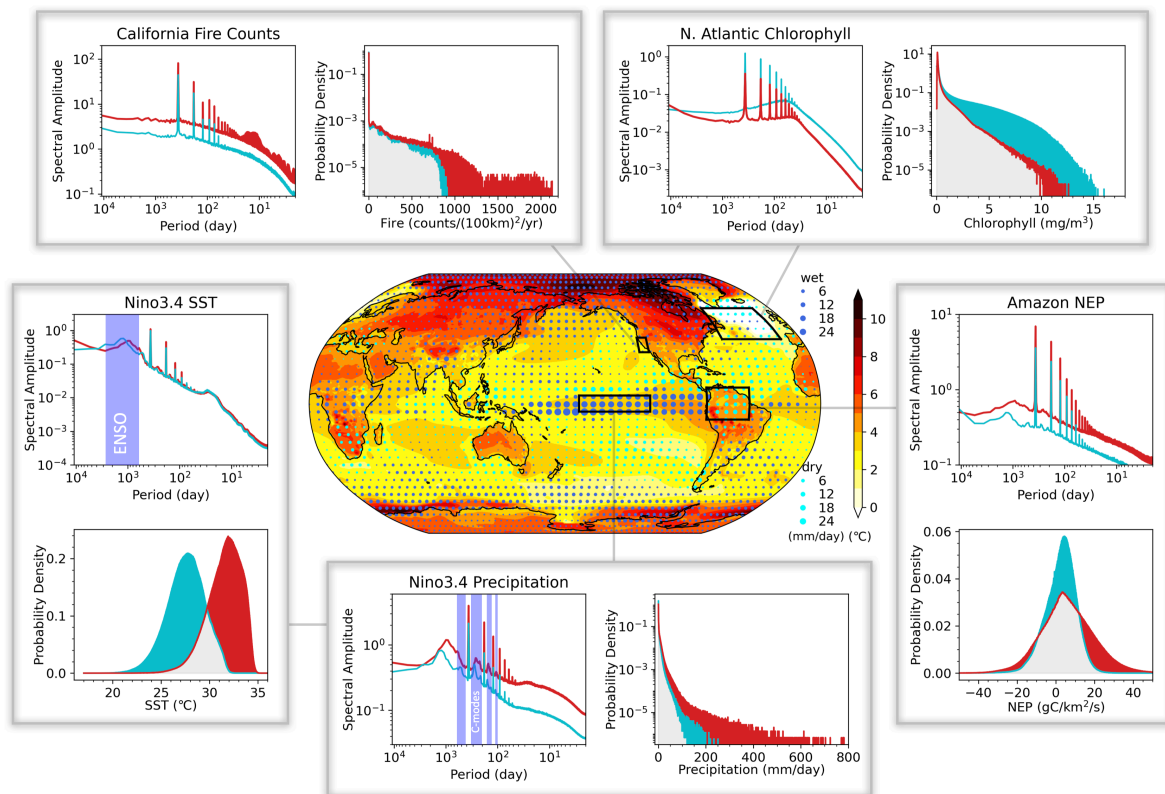


Fig. 2. Changes in the Fourier amplitude spectrum of historical (1960-1989) to future (2070-2099) climate variability in CESM2-LE. The center map shows historical-to-future changes in surface temperature (shaded, °C) and precipitation (solid blue dots, mm day⁻¹). Each pairing of panels shows historical (cyan) and future (red) spectra and PDFs for five different variables over four different regions. The spectra are considered over the respective periods 1960-1989 (historical) and 2070-2099 (future), thereby including the trend, and PDFs are considered for all 365 days of 1989 and 2099 to minimize the impact of the trend. From upper-left clockwise, each pair of panels shows the historical (blue) and future (red) number of fire occurrences in California (32°N-41°N, 125°W-118°W, land only), surface chlorophyll concentration in the North Atlantic subpolar gyre (40°N-60°N, 60°W-15°W), net ecosystem production (NEP) in the Amazon (10°S-10°N, 80°W-50°W, land-only), precipitation over the Niño3.4 region (5°S-5°N, 170°W-120°W), and sea surface temperature over the Niño3.4 region. The spectra are calculated for daily timeseries at individual grid points including forced responses and internal variability and using 30-year intervals. Subsequently the spectra are averaged over the grid points in each region (see Methods). Sharp spectral peaks are associated with the annual cycle and its non-sinusoidal components, which generate high order harmonics. Shaded areas for spectra of precipitation and temperature in the Niño3.4 region correspond to the timescales of the El Niño-Southern Oscillation (ENSO) and ENSO-annual cycle combination modes (7I) (C-modes). Spectra are shown as amplitude, with the units being the same as the x-axes for the PDFs. PDFs of positive-definite variables (California fire counts, N. Atlantic surface chlorophyll, and Niño3.4 precipitation) are shown with logarithmic y-axes. The fields in the center panel are presented in more detail in fig. S4, except that there 2m reference temperature is used rather than surface temperature. A suite of complementary spectral and PDF analyses to those shown here are presented in fig. S5.

94
95
96
97
98
99
00
01
02
03
04
05
06
07
08
09
10
11
12
13
14
15
16
17
18
19
20
21

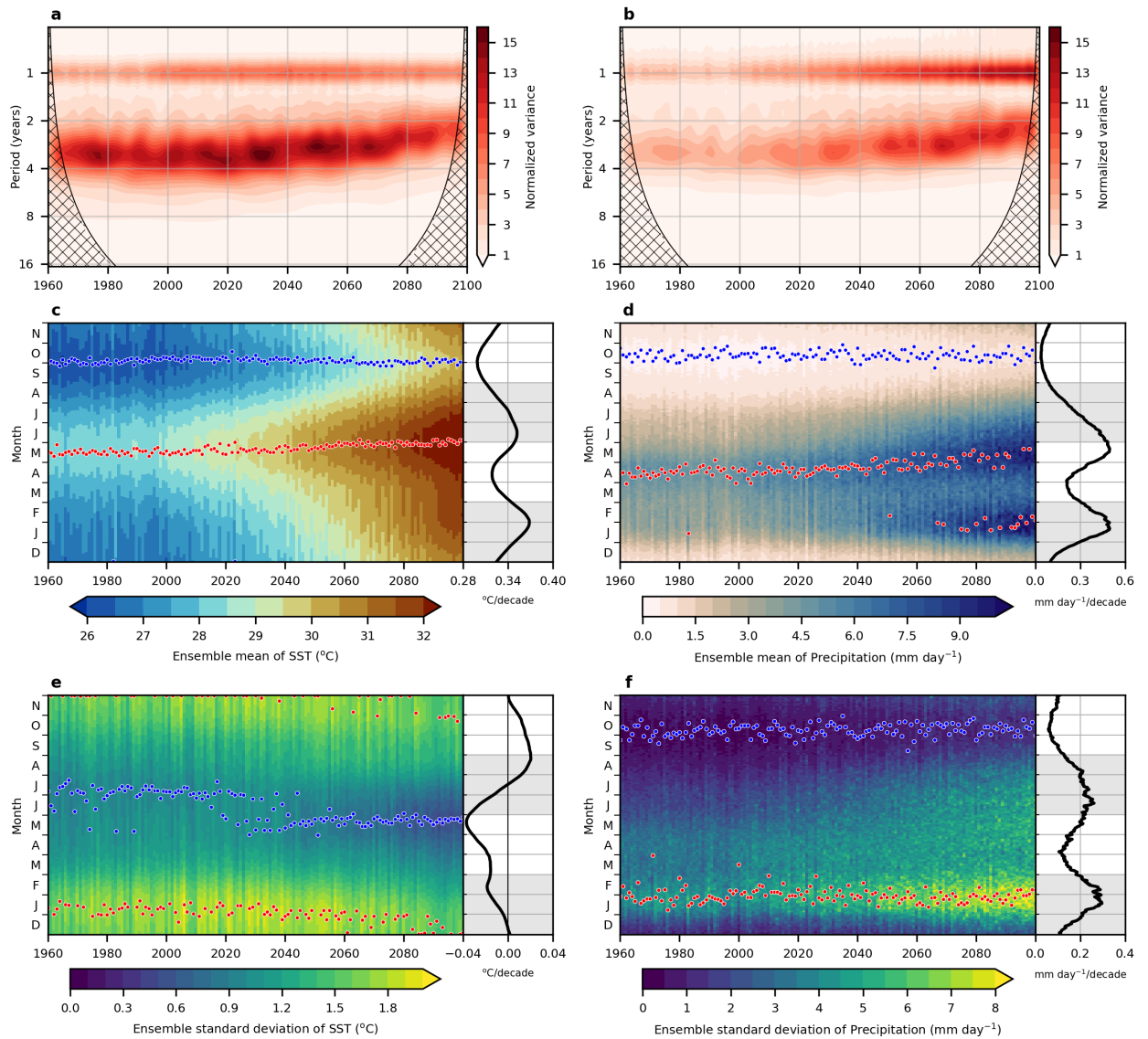


Fig. 3. Changes in the dominant frequencies, seasonal mean, and seasonal variance of sea surface temperature (SST, left) and precipitation (right), in the Niño3.4 region (5°S-5°N, 170°W-120°W). (Top) The wavelet power spectra of Niño3.4 (a) SST and (b) precipitation using a Morlet wavelet, normalized by $\bar{\sigma}^{-2}$, where $\bar{\sigma}$ is the ensemble mean standard deviation of the respective Niño3.4 time series (63). The y axis shows the equivalent Fourier period in years. The hatching indicates regions where the wavelet spectrum is not trustworthy due to edge effects. Prior to calculating the wavelet spectra, the time series were detrended by subtracting the ensemble-mean annual means, which were linearly interpolated to a monthly timestep. (Middle) The ensemble-mean of Niño 3.4 (c) SST and (d) precipitation indicated for each day (ordinate) and year (abscissa) using daily output. The red/blue dots indicate the maximum/minimum daily values of each year. The black line to the right in panels (c)-(f) indicates the linear trend over 1960-2100. (Bottom) Same as for (c) and (d), but for the cross-ensemble standard deviations of (e) SST and (f) precipitation.

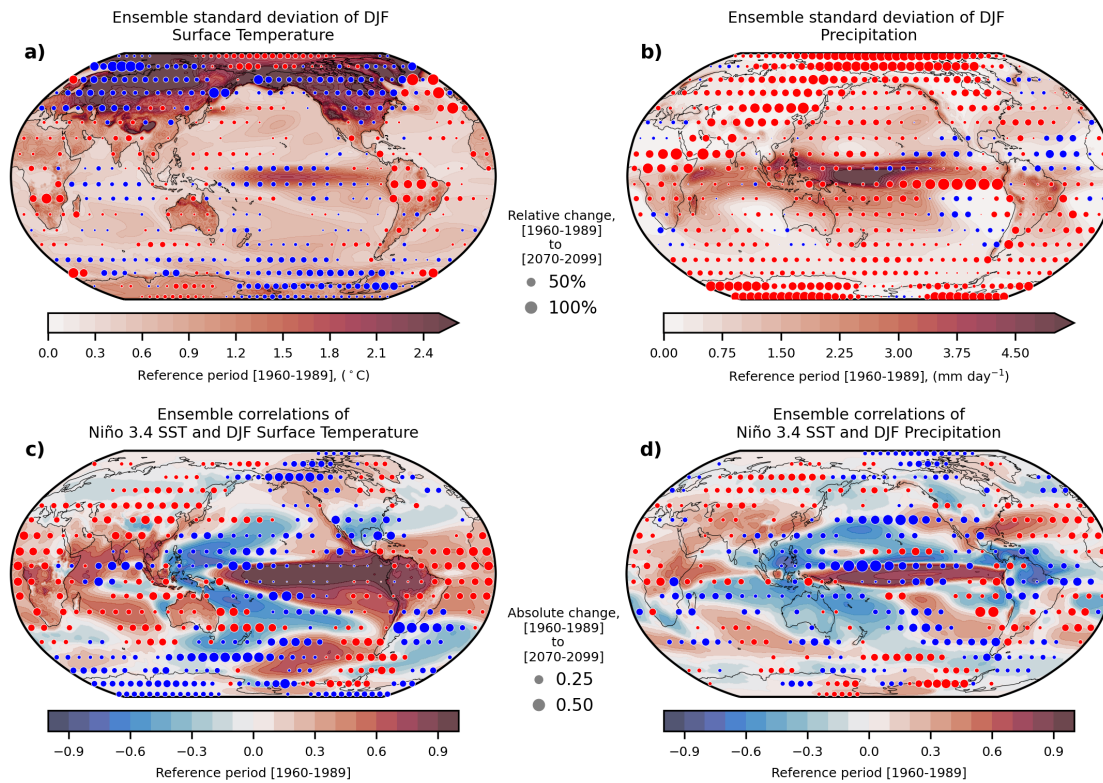
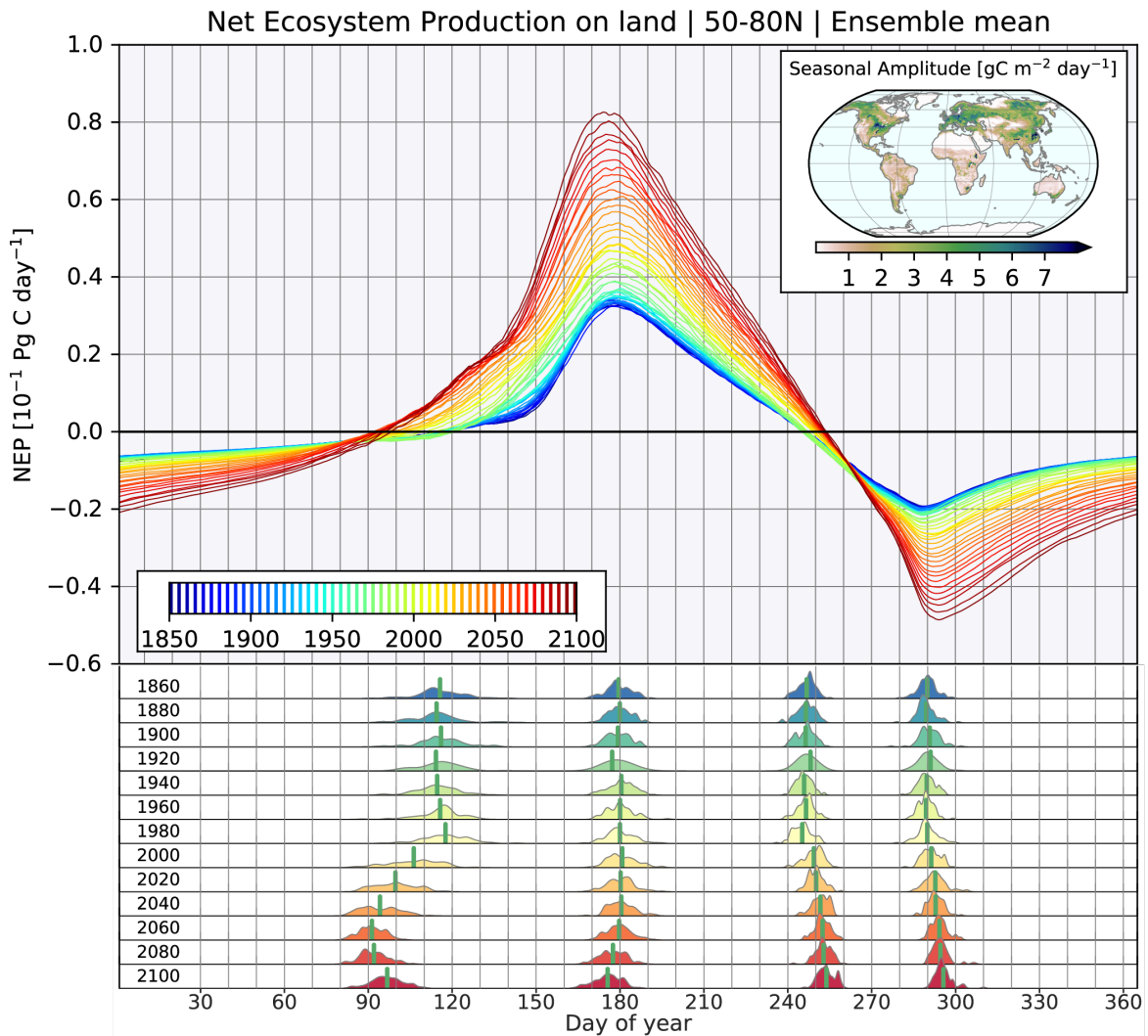


Fig. 4. Changes in the patterns of interannual variability and Niño 3.4 correlation coefficients of December-January-February (DJF) surface temperature and precipitation. (Top) Color shading shows the time-averaged absolute cross-ensemble standard deviation of the DJF seasonal mean surface temperature (a) and precipitation (b) for the period 1960-1989. Circles show the relative changes in the standard deviations between 2070-2099 and 1960-1989, where insignificant change ($p \geq 0.05$) has been removed. Statistical significance of the changes (circles) was determined based on the p -values of the two-sample Welch's t -tests for the equality of temporal means of the ensemble standard deviations, with the equivalent sample sizes adjusted to account for serial correlations (Methods). (Bottom) Color shading shows ensemble-wise correlations of the Niño3.4 index with surface temperature (c) and precipitation (d) anomalies for DJF, averaged over the period 1960-1989. Circles show the absolute change in correlations between 2070-2099 and 1960-1989, where statistically insignificant change ($p \geq 0.05$) has been removed. The Niño3.4 index for ENSO is the spatial average of sea surface temperature within 5°S-5°N, 170°W-120°W. Statistical significance of the changes (circles) was determined based on the p -values of two-sample Student's t -test of the Fisher z -transformed correlation coefficients (72). Note that the t -test treats the ensemble standard deviations and correlations as stationary and serially uncorrelated with either of the two periods. For all four panels, the circles represent subsampled fields at 10° intervals over the global domain. The corresponding analysis for June-July-August (JJA) is presented in fig. S6.



61
 62
 63
 64
 65
 66
 67
 68
 69
 70
 71
 72
 73
 74
 75
 76
 77
 78
 79

Fig. 5. Expansion of growing season length, or equivalently the carbon uptake period, over 50°N-80°N (shown here for all 90 members for which daily-mean land output was saved). Upper panel: Evolution of ensemble mean seasonal cycle (one line for every five years, color-coded) of integrated net ecosystem productivity (NEP), with positive values indicating net terrestrial carbon uptake and negative values indicating loss of carbon from the aggregated land region. The first zero crossing marks the start of the growing season, and the second zero crossing marks the end of the growing season; Lower panel: Histograms of first occurrence of zero crossing, peak, second zero crossing, and minimum as a function of the day of year. The horizontal axis for both panels is a climatological calendar year, and aggregation is done across 90 members. The histograms represent model output sampled at 20-year intervals. The inlay map (upper right) shows the ensemble mean amplitude of the seasonal cycle of NEP averaged over 1960-1989 ($\text{gC m}^{-2} \text{day}^{-1}$).

References

1. E. S. Sarachik, paper presented at the Second International Conference on Climate, Sustainability, and Development in Semi-Arid Regions, Fortaleza, Brazil, 2010.
2. K. Hasselmann, Stochastic Climate Models. 1. Theory. *Tellus* **28**, 473-485 (1976).
3. C. L. E. Franzke *et al.*, The Structure of Climate Variability Across Scales. *Reviews of Geophysics* **58**, 44 (2020).
4. M. F. Stuecker, F. F. Jin, A. Timmermann, El Nino-Southern Oscillation frequency cascade. *Proceedings of the National Academy of Sciences of the United States of America* **112**, 13490-13495 (2015).
5. A. Timmermann *et al.*, Increased El Nino frequency in a climate model forced by future greenhouse warming. *Nature* **398**, 694-697 (1999).
6. W. J. Cai *et al.*, Increased variability of eastern Pacific El Nino under greenhouse warming. *Nature* **564**, 201-+ (2018).
7. C. Deser *et al.*, Insights from Earth system model initial-condition large ensembles and future prospects. *Nature Climate Change* **10**, 277-+ (2020).
8. S. Schlunegger *et al.*, Time of Emergence and Large Ensemble Intercomparison for Ocean Biogeochemical Trends. *Global Biogeochemical Cycles* **34**, 18 (2020).
9. H. Zelle, G. J. Van Oldenborgh, G. Burgers, H. Dijkstra, El Nino and Greenhouse warming: Results from ensemble simulations with the NCAR CCSM. *Journal of Climate* **18**, 4669-4683 (2005).
10. S. Drijfhout, W. Hazeleger, F. Selten, R. Haarsma, Future changes in internal variability of the Atlantic Meridional Overturning Circulation. *Climate Dynamics* **30**, 407-419 (2008).
11. G. Branstator, F. Selten, "Modes of Variability" and Climate Change. *Journal of Climate* **22**, 2639-2658 (2009).
12. D. Rind, R. Goldberg, R. Ruedy, Change in Climate Variability in the 21st-Century. *Climatic Change* **14**, 5-37 (1989).
13. J. Raisanen, CO₂-induced changes in interannual temperature and precipitation variability in 19 CMIP2 experiments. *Journal of Climate* **15**, 2395-2411 (2002).
14. C. Huntingford, P. D. Jones, V. N. Livina, T. M. Lenton, P. M. Cox, No increase in global temperature variability despite changing regional patterns. *Nature* **500**, 327-330 (2013).
15. J. A. Screen, Arctic amplification decreases temperature variance in northern mid- to high-latitudes. *Nature Climate Change* **4**, 577-582 (2014).
16. R. J. Stouffer, R. T. Wetherald, Changes of variability in response to increasing greenhouse gases. Part I: Temperature. *Journal of Climate* **20**, 5455-5467 (2007).
17. R. T. Wetherald, Changes of Variability in Response to Increasing Greenhouse Gases. Part II: Hydrology. *Journal of Climate* **22**, 6089-6103 (2009).
18. A. G. Pendergrass, R. Knutti, F. Lehner, C. Deser, B. M. Sanderson, Precipitation variability increases in a warmer climate. *Scientific Reports* **7**, 9 (2017).
19. N. Maher *et al.*, The Max Planck Institute Grand Ensemble: Enabling the Exploration of Climate System Variability. *Journal of Advances in Modeling Earth Systems* **11**, 2050-2069 (2019).
20. T. Haszpra, M. Herein, T. Bodai, Investigating ENSO and its teleconnections under climate change in an ensemble view - a new perspective. *Earth System Dynamics* **11**, 267-280 (2020).
21. N. Maher, S. B. Power, J. Marotzke, More accurate quantification of model-to-model agreement in externally forced climatic responses over the coming century. *Nature Communications* **12**, 13 (2021).
22. G. Danabasoglu *et al.*, The Community Earth System Model Version 2 (CESM2). *Journal of Advances in Modeling Earth Systems* **12**, 35 (2020).

23. I. R. Simpson *et al.*, An Evaluation of the Large-Scale Atmospheric Circulation and Its Variability in CESM2 and Other CMIP Models. *Journal of Geophysical Research-Atmospheres* **125**, 42 (2020).
24. J. T. Fasullo, Evaluating simulated climate patterns from the CMIP archives using satellite and reanalysis datasets using the Climate Model Assessment Tool (CMATv1). *Geoscientific Model Development* **13**, 3627-3642 (2020).
25. S. Milinski, N. Maher, D. Olonscheck, How large does a large ensemble need to be? *Earth System Dynamics* **11**, 885-901 (2020).
26. L. Kwiatkowski *et al.*, Twenty-first century ocean warming, acidification, deoxygenation, and upper-ocean nutrient and primary production decline from CMIP6 model projections. *Biogeosciences* **17**, 3439-3470 (2020).
27. V. K. Arora *et al.*, Carbon-concentration and carbon-climate feedbacks in CMIP6 models and their comparison to CMIP5 models. *Biogeosciences* **17**, 4173-4222 (2020).
28. A. Gettelman *et al.*, High Climate Sensitivity in the Community Earth System Model Version 2 (CESM2). *Geophysical Research Letters* **46**, 8329-8337 (2019).
29. W. Weijer, W. Cheng, O. A. Garuba, A. Hu, B. T. Nadiga, CMIP6 Models Predict Significant 21st Century Decline of the Atlantic Meridional Overturning Circulation. *Geophysical Research Letters* **47**, (2020).
30. K. B. Rodgers *et al.*, Reemergence of Anthropogenic Carbon Into the Ocean's Mixed Layer Strongly Amplifies Transient Climate Sensitivity. *Geophysical Research Letters* **47**, 9 (2020).
31. K. Toyama *et al.*, Large Reemergence of Anthropogenic Carbon into the Ocean's Surface Mixed Layer Sustained by the Ocean's Overturning Circulation. *Journal of Climate* **30**, 8615-8631 (2017).
32. R. Revelle, H. E. Suess, Carbon Dioxide Exchange Between Atmosphere and Ocean and the Question of an Increase of Atmospheric CO₂ During the Past Two Decades. *Tellus* **9**, 18-27 (1957).
33. S.-P. Xie *et al.*, Global Warming Pattern Formation: Sea Surface Temperature and Rainfall. *Journal of Climate* **23**, 966-986 (2010).
34. H. Goosse *et al.*, Quantifying climate feedbacks in polar regions. *Nature communications* **9**, 1-13 (2018).
35. E. S. Chung *et al.*, Cold-Season Arctic Amplification Driven by Arctic Ocean-Mediated Seasonal Energy Transfer. *Earths Future* **9**, (2021).
36. S. Rahmstorf *et al.*, Exceptional twentieth-century slowdown in Atlantic Ocean overturning circulation. *Nature Climate Change* **5**, 475-480 (2015).
37. M. B. Menary, R. A. Wood, An anatomy of the projected North Atlantic warming hole in CMIP5 models. *Climate Dynamics* **50**, 3063-3080 (2018).
38. T. Stocker, W. G. I. Intergovernmental Panel on Climate Change, WMO, UNEP. (Cambridge University Press, Cambridge, United Kingdom, and New York, NY, USA, 2013).
39. S. T. Kim *et al.*, Response of El Nino sea surface temperature variability to greenhouse warming. *Nature Climate Change* **4**, 786-790 (2014).
40. K.-S. Yun *et al.*, **Increasing ENSO-rainfall variability due to changes in future tropical temperature-rainfall relationship.** *Communications Earth & Environment* **2**, 10.1038/s43247-43021-00108-43248 (2021).
41. S. S. Renner, C. M. Zohner, Climate Change and Phenological Mismatch in Trophic Interactions Among Plants, Insects, and Vertebrates. *Annual Review of Ecology, Evolution, and Systematics* **49**, 165-182 (2018).
42. Z. C. Zhu *et al.*, Greening of the Earth and its drivers. *Nature Climate Change* **6**, 791-+ (2016).
43. I. H. Myers-Smith *et al.*, Complexity revealed in the greening of the Arctic. *Nature Climate Change* **10**, 106-117 (2020).

- 84 44. D. M. Lawrence *et al.*, The Community Land Model Version 5: Description of New
85 Features, Benchmarking, and Impact of Forcing Uncertainty. *Journal of Advances in*
86 *Modeling Earth Systems* **11**, 4245-4287 (2019).
- 87 45. D. L. Lombardozzi *et al.*, Simulating Agriculture in the Community Land Model
88 Version 5. *Journal of Geophysical Research-Biogeosciences* **125**, 19 (2020).
- 89 46. G. Hegerl, C *et al.*, in *Climate Change 2007: The Physical Science Basis. Contribution*
90 *of Working Group I to the Fourth Assessment Report of the Intergovernmental Panel*
91 *on Climate Change [Solomon, S., D. Qin, M. Manning, Z. Chen, M. Marquis, K.B.*
92 *Averyt, M. Tignor and H.L. Miller (eds.)]. Cambridge University Press, Cambridge,*
93 *United Kingdom and New York, NY, USA.* (2007).
- 94 47. D. Diaz, F. Moore, Quantifying the economic risks of climate change. *Nature Climate*
95 *Change* **7**, 774-782 (2017).
- 96 48. V. Eyring *et al.*, Overview of the Coupled Model Intercomparison Project Phase 6
97 (CMIP6) experimental design and organization. *Geoscientific Model Development* **9**,
98 1937-1958 (2016).
- 99 49. B. C. O'Neill *et al.*, The Scenario Model Intercomparison Project (ScenarioMIP) for
00 CMIP6. *Geoscientific Model Development* **9**, 3461-3482 (2016).
- 01 50. R. Smith *et al.*, The parallel ocean program (POP) reference manual ocean component
02 of the community climate system model (CCSM) and community earth system model
03 (CESM). *LAUR-01853* **141**, 1-140 (2010).
- 04 51. D. A. Bailey, M. M. Holland, A. K. DuVivier, E. C. Hunke, A. K. Turner, Impact of a
05 New Sea Ice Thermodynamic Formulation in the CESM2 Sea Ice Component. *Journal*
06 *of Advances in Modeling Earth Systems* **12**, 15 (2020).
- 07 52. Q. Li *et al.*, Langmuir mixing effects on global climate: WAVEWATCH III in CESM.
08 *Ocean Modelling* **103**, 145-160 (2016).
- 09 53. A. Gettelman, H. Morrison, Advanced Two-Moment Bulk Microphysics for Global
10 Models. Part I: Off-Line Tests and Comparison with Other Schemes. *Journal of*
11 *Climate* **28**, 1268-1287 (2015).
- 12 54. J. K. Moore, S. C. Doney, J. A. Kleypas, D. M. Glover, I. Y. Fung, An intermediate
13 complexity marine ecosystem model for the global domain. *Deep-Sea Research Part*
14 *Ii-Topical Studies in Oceanography* **49**, 403-462 (2001).
- 15 55. J. K. Moore, S. C. Doney, K. Lindsay, Upper ocean ecosystem dynamics and iron
16 cycling in a global three-dimensional model. *Global Biogeochemical Cycles* **18**, 21
17 (2004).
- 18 56. J. K. Moore, K. Lindsay, S. C. Doney, M. C. Long, K. Misumi, Marine Ecosystem
19 Dynamics and Biogeochemical Cycling in the Community Earth System Model
20 CESM1(BGC) : Comparison of the 1990s with the 2090s under the RCP4.5 and
21 RCP8.5 Scenarios. *Journal of Climate* **26**, 9291-9312 (2013).
- 22 57. G. B. Bonan *et al.*, Model Structure and Climate Data Uncertainty in Historical
23 Simulations of the Terrestrial Carbon Cycle (1850-2014). *Global Biogeochemical*
24 *Cycles* **33**, 1310-1326 (2019).
- 25 58. F. Li, S. Levis, D. S. Ward, Quantifying the role of fire in the Earth system - Part 1:
26 Improved global fire modeling in the Community Earth System Model (CESM1).
27 *Biogeosciences* **10**, 2293-2314 (2013).
- 28 59. F. Li, D. M. Lawrence, Role of Fire in the Global Land Water Budget during the
29 Twentieth Century due to Changing Ecosystems. *Journal of Climate* **30**, 1893-1908
30 (2017).
- 31 60. N. Collier *et al.*, The International Land Model Benchmarking (ILAMB) System:
32 Design, Theory, and Implementation. *Journal of Advances in Modeling Earth Systems*
33 **10**, 2731-2754 (2018).
- 34 61. J. E. Kay *et al.*, The Community Earth System Model (CESM) Large Ensemble
35 Project: A Community Resource for Studying Climate Change in the Presence of
36 Internal Climate Variability. *Bulletin of the American Meteorological Society* **96**,
37 1333-1349 (2015).

- '38 62. M. J. E. van Marle *et al.*, Historic global biomass burning emissions for CMIP6
'39 (BB4CMIP) based on merging satellite observations with proxies and fire models
'40 (1750-2015). *Geoscientific Model Development* **10**, 3329-3357 (2017).
- '41 63. C. Torrence, G. P. Compo, A practical guide to wavelet analysis. *Bulletin of the*
'42 *American Meteorological Society* **79**, 61-78 (1998).
- '43 64. N. G. Loeb *et al.*, Toward Optimal Closure of the Earth's Top-of-Atmosphere
'44 Radiation Budget. *Journal of Climate* **22**, 748-766 (2009).
- '45 65. R. F. Adler *et al.*, The version-2 global precipitation climatology project (GPCP)
'46 monthly precipitation analysis (1979-present). *Journal of Hydrometeorology* **4**, 1147-
'47 1167 (2003).
- '48 66. R. F. Adler, G. J. Gu, G. J. Huffman, Estimating Climatological Bias Errors for the
'49 Global Precipitation Climatology Project (GPCP). *Journal of Applied Meteorology and*
'50 *Climatology* **51**, 84-99 (2012).
- '51 67. L. A. Roach *et al.*, Antarctic Sea Ice Area in CMIP6. *Geophysical Research Letters* **47**,
'52 10 (2020).
- '53 68. M. Ishii *et al.*, Accuracy of Global Upper Ocean Heat Content Estimation Expected
'54 from Present Observational Data Sets. *Sola* **13**, 163-167 (2017).
- '55 69. F. Fetterer, K. Knowles, W. Meier, M. Savoie, A. Windnagel. (2017).
- '56 70. E. Frajka-Williams *et al.*, Atlantic Meridional Overturning Circulation: Observed
'57 Transport and Variability. *Frontiers in Marine Science* **6**, (2019).
- '58 71. M. F. Stuecker, A. Timmermann, F. F. Jin, S. McGregor, H. L. Ren, A combination
'59 mode of the annual cycle and the El Nino/Southern Oscillation. *Nature Geoscience* **6**,
'60 540-544 (2013).
- '61 72. A. Timmermann, J. Sachs, O. E. Timm, Assessing divergent SST behavior during the
'62 last 21 ka derived from alkenones and G. ruber-Mg/Ca in the equatorial Pacific.
'63 *Paleoceanography* **29**, 680-696 (2014).
- '64
'65
'66

67 **Acknowledgments**

68 The CESM2 Large Ensemble (CESM2-LE) simulations presented here for the first time have
69 been conducted through a partnership between the IBS Center for Climate Physics (ICCP) in
70 South Korea and the Community Earth System Model (CESM) group at the National Center for
71 Atmospheric Research (NCAR) in the US, representing a broad collaborative effort between
72 scientists from both centers.

73 The authors would like to thank Woncheol Roh at the ICCP and John Fasullo, Keith Lindsay,
74 Adam S. Phillips, and Gary Strand at NCAR for their input and support. We would also like to
75 thank all of the other scientists, software engineers, and administrators at both NCAR and the
76 ICCP that contributed to this project. The framework for the macro- and micro-perturbation
77 initialization strategy employed here also benefited from the US CLIVAR Workshop on Large
78 Ensembles held July 2019 in Boulder CO, USA.

79 The CESM project is supported primarily by the US National Science Foundation (NSF). This
80 material is based upon work supported by the NCAR, which is a major facility sponsored by
81 the US NSF under Cooperative Agreement 1852977. The CESM2 pre-industrial control
82 simulation was performed on the Cheyenne supercomputer (doi:10.5065/D5RX99HX) operated
83 by the Computational and Information Systems Laboratory (CISL) at NCAR.

84 The simulations presented here were conducted on the IBS/ICCP supercomputer “Aleph”, a
85 1.43-petaflop high-performance Cray XC50-LC Skylake computing system with 18,720
86 processor cores, with 9.59-petabytes of disc storage, and 43-petabytes of tape archive storage.
87 The 15-month long simulations generated 5.3 Petabyte of data and used approximately 200
88 million CPU hours computing time.

89 **Funding**

91 The work of K.B.R., S.-S.L., A.T., R.Y., J.-E.K., K.S. and L.H. was supported by the Institute
92 for Basic Sciences (IBS), Republic of Korea, under IBS-R028-D1. T.B. was supported by the
93 Institute for Basic Sciences (IBS), Republic of Korea, under IBS-R028-Y1. M.F.S. was
94 supported by NOAA’s Climate Program Office’s Modeling Analysis, Predictions, and
95 Projections (MAPP) program, grant NA20OAR4310445 and participates in the MAPP Marine
96 Ecosystem Task Force. This is IPRC publication X and SOEST contribution Y. W.R.W and
97 D.L.L were supported by the National Institute of Food and Agriculture, US Department of
98 Agriculture (2015-67003-23485). W.R.W. was also supported by NASA Interdisciplinary
99 Science Program award NNX17AK19G. The work of N.R was supported by the Regional and
:00 Global Model Analysis (RGMA) component of the Earth and Environmental System Modeling
:01 Program of the U.S. Department of Energy's Office of Biological & Environmental Research
:02 (BER) via National Science Foundation IA 1947282.

:03 **Author Contributions**

:04 The CESM2-LE project was initiated by K.B.R., A.T., G.D., and C.D. The scientific framing
:05 of this manuscript was developed by K.B.R., A.T., J.-E. K., R.Y., K.S., S.-S. L., and M.F.S.
:06 Analyses and scientific post-processing were performed by R.Y., J.-E. K., K.S., L. H., T.B., and
:07 W.K. The CESM2-LE model runs were set up, performed, and extracted through a joint effort
:08 of the team S.-S.L, N.R., and J.E. The initialization procedure for the model was developed
:09 through the joint efforts of C.D., G.D., I.S., W.K. S.G.Y, and N.R. All authors discussed the
:10 results and contributed to the writing of the manuscript.
:11

:12
:13
:14
:15
:16
:17
:18
:19
:20
:21
:22
:23
:24
:25

Competing Interests

The authors declare that they have no competing interests.

Data and materials availability

The CESM2-LE model output will first become available through <https://www.cesm.ucar.edu/projects/community-projects/LENS2/> on June 14th 2021. A subset of commonly-used variables will also be made available on June 14th through the ICCP climate data openDAP server (<https://climatedata.ibs.re.kr>). Analysis scripts used to produce the figures in this manuscript will be made available through GitHub and <https://climatedata.ibs.re.kr>, including the data analysis presented in **Fig. 1**.

Supplementary Materials for

Ubiquity of human-induced changes in climate variability

Keith B Rodgers*, Sun-Seon Lee, Nan Rosenbloom, Axel Timmermann*, Gokhan Danabasoglu, Clara Deser, Jim Edwards, Ji-Eun Kim, Isla Simpson, Karl Stein, Malte F. Stuecker, Ryohei Yamaguchi, Tamas Bodai, Eui-Seok Chung, Lei Huang, Who M. Kim, Jean-François Lamarque, Danica L. Lombardozzi, William R. Wieder, Stephen G. Yeager

*Corresponding authors: krodgers@pusan.ac.kr ; axel@ibsclimate.org

This PDF file includes:

Supplementary Text
Figs. S1 to S6

Supplementary Text

For the analysis in **Fig. 1** for sea-ice, daily mean fields were used for both the model and data product. In representing sea ice extent threshold of 15% was used, whereby each grid cell is identified as being ice-covered. For the net land fluxes of CO₂, we have used the variable net biome production, which includes the effects of not only photosynthesis and respiration, but also fire and land-use change.

For the spectral analysis in **Fig. 2**, each Fast Fourier Transform (FFT) spectrum is calculated for the time series of raw data over a given variable for the full 35-year interval. This includes all timescales shorter than 35 years and longer than 2 days (months) for daily (monthly) time-resolution data. The spectrum is calculated first at each horizontal grid point and for each ensemble member, and then averaged over the designated region and over the 100 ensemble members. The spectral calculations are performed to represent amplitudes of signals. AMOC is defined as a maximum transport at 40°N. For the spectrum of internal variability of AMOC, the ensemble mean is subtracted from the raw data to remove a forced response. The surface chlorophyll fields analyzed here represent total chlorophyll concentrations, taken as a sum of diatom, diazotroph, and small phytoplankton chlorophyll.

The analysis of patterns of variance and covariance in **Fig. 3** uses cross-ensemble calculations of annual mean standard deviations, with the cross-ensemble calculations applied for identical time records for each ensemble member. For the case of precipitation averaged over December, January, February (DJF) (**Fig. 3a**) and surface temperature for DJF (**Fig. 3b**), the standard deviations calculated separately over all years spanning 1960-1989 and 2070-2099 were first calculated, and then averaged over the two respective periods, with the figures showing the difference in standard deviation between these periods. The panels corresponding to changes in correlation between Niño3.4 (170°W-120°W, 5°N-5°S) SST anomalies and precipitation (**Fig. 3c**) and surface temperature (**Fig. 3d**) are first calculated separately across ensemble members for each year, and then averaged for the two respective periods (1960-1989 and 2070-2099) before taking the differences. This calculation of both standard deviations and correlations across the ensemble dimension harnesses the full power of the large ensemble, and is analogous to the empirical orthogonal function (EOF) EOF-E snapshot method applied with empirical orthogonal functions (EOFs)⁶⁷.

For **Fig. 4**, the wavelet power spectra of Niño3.4 (a) SST and (b) precipitation was calculated using a Morlet wavelet, normalized by $\bar{\sigma}^{-2}$, where $\bar{\sigma}$ is the ensemble mean standard deviation of the respective Niño3.4 time series. Prior to calculating the wavelet spectra, the time series were detrended by subtracting the ensemble-mean annual means, which were linearly interpolated to a monthly timestep.

For the seasonality/phenology analysis in the upper panel of Fig. 5, an area-integral of daily-mean net ecosystem production ($NEP=GPP-ER$, or the difference between gross primary production and ecosystem respiration) is performed over the domain $50^{\circ}N-80^{\circ}N$ for each ensemble member separately. A total of 90 ensemble members are used for this calculation, as daily CLM5 output was not saved for the first 10 members, namely 1001.001, 1021.002, 1041.003, 1061.004, 1081.005, 1101.006, 1121.007, 1141.008, 1161.009, and 1181.010. For NEP the first task is to identify the timing of the transition in spring from net carbon release to net carbon gain by the terrestrial system (first zero crossing), the subsequent autumn transition from net carbon uptake to carbon release (second zero crossing), as well as the timing of maximum positive and maximum negative NEP. Due to internal variability, these markers of seasonal phasing (**Fig. 5**, lower panel) are different between ensemble members, and thus these are tabulated for the individual members prior to calculating the ensemble mean.

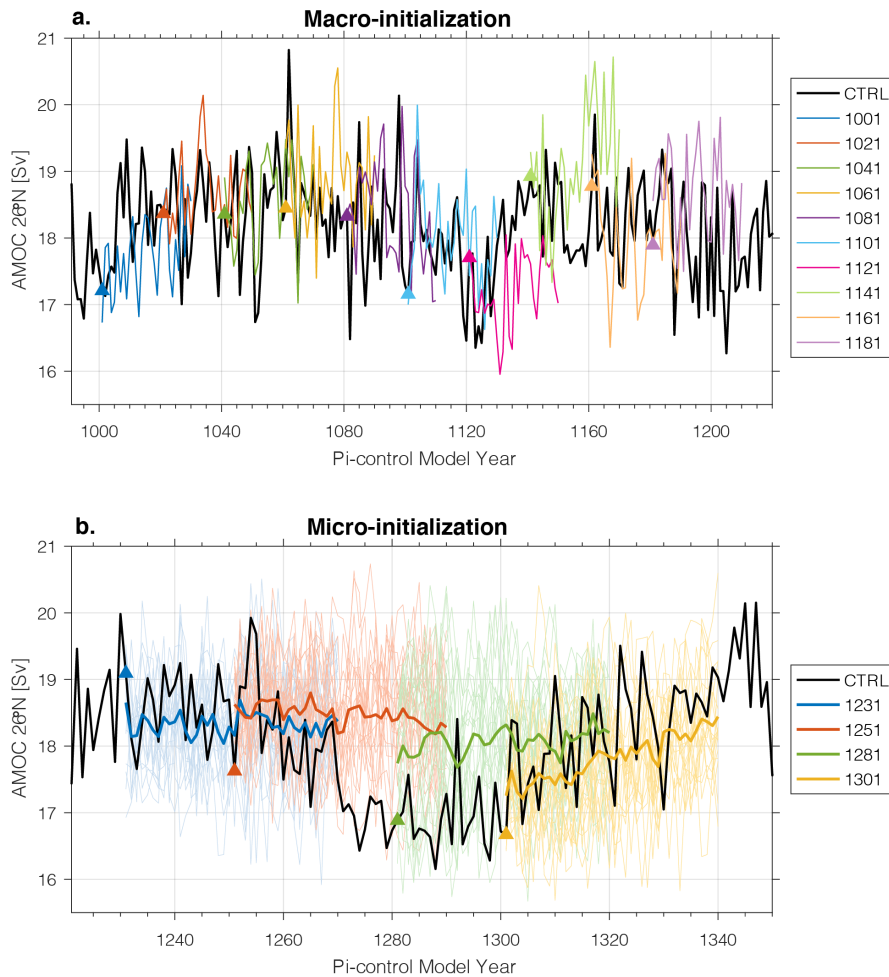


Fig. S1.

CESM2 LE initialization consequences for the Atlantic Meridional Overturning Circulation (AMOC). The AMOC transport in the pre-industrial control simulation (black line) for CESM2 (*I*) is shown over two time slices corresponding to (a) 10 of the 20 macro-initializations and (b) the micro-initializations, as described in Methods. In panel (a) the AMOC transports for the individual ensemble members are shown as solid colors, with the initiation points marked as colored triangles. In panel (b) the AMOC transports are shown in thin solid lines for individual ensemble members, and the ensemble-mean is represented as a thicker solid line.

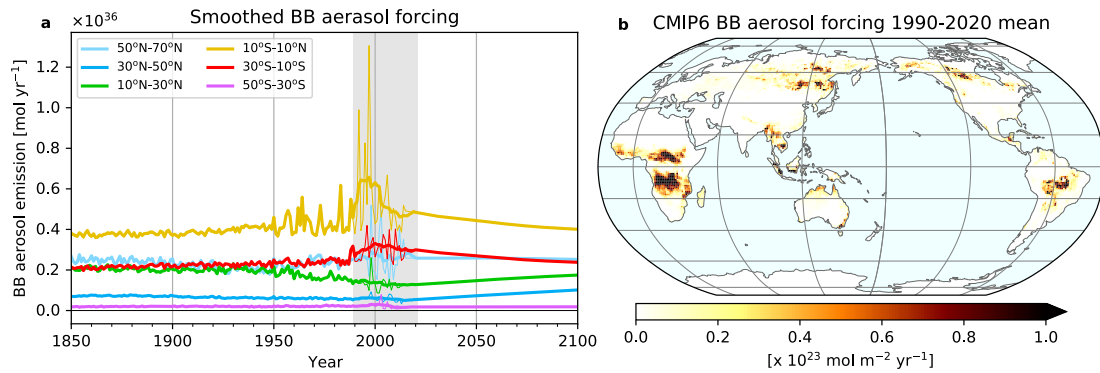


Fig. S2.

Biomass burning. (a) Net surface aerosol fluxes (sum of six components) associated with biomass burning (2) are shown integrated over latitude bands, corresponding to the fluxes used for the ensemble members 1-50 (color-coded light lines), and then the temporally smoothed fields are used for ensemble members 51-100 (color-coded bold lines). Smoothing is applied with an 11-year running-mean filter, with the averaging procedure impacting variability over the period 1990-2020, applied separately for each month to preserve the integrity of the seasonal cycle, and (b) map of mean total aerosol fluxes associated with biomass burning fluxes used for the first 50 ensemble members. The smoothing procedure applied for biomass burning is described in the Methods section. The total net surface aerosol flux is nearly conserved between the two subsets of ensembles.

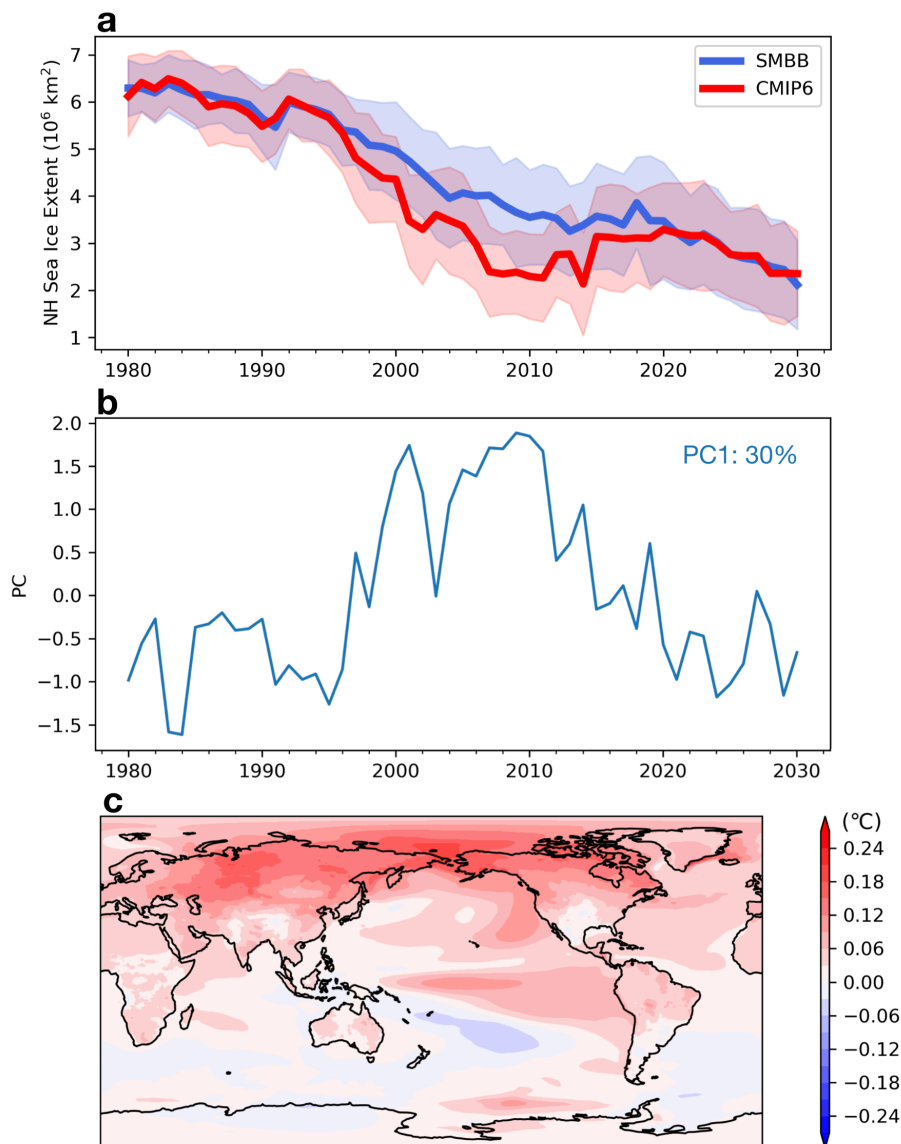


Fig. S3.

Impact of biomass burning perturbations on the mean state. The impact of the smoothed biomass on the mean state evolution of the model is considered for Northern Hemisphere sea-ice extent and global surface temperatures, with the 50 simulations with the original forcing (CMIP6) compared with the 50 simulations with smoothed biomass burning fluxes (SMBB). For sea ice extent in September (a) the ensemble mean for CMIP6 (thick red line) reveals a steeper decrease from the early 1990s before recovering during the 2010s and eventually converging with the SMBB case (thick blue line). Lighter shading for both SMBB and CMIP6 indicates 1-

SD variations. For surface temperature differences, EOF analysis has been applied to the annual mean difference in the ensemble mean, with (b) the first PC and (c) the first EOF, considered over 1980-2030.

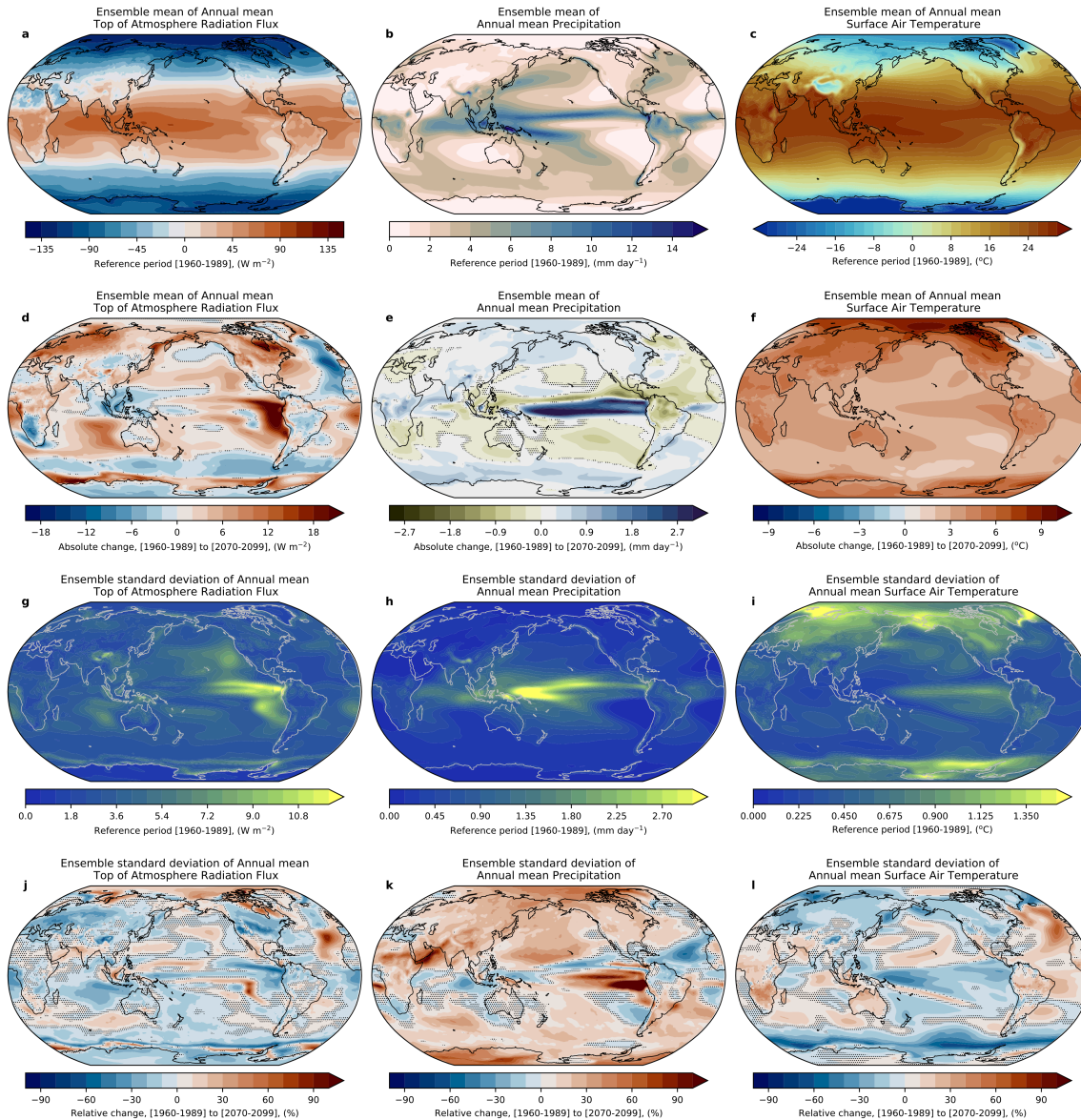


Fig. S4.

Patterns of change in CESM2 LE. First column: net top of the atmosphere radiative flux; Second column: precipitation; Third column: surface temperature. First row: Mean state averaged over 1960-1989; Second Row: Change in mean state between 1960-1989 and 2070-2099; Third row: Average over 1960-1989 of snapshot (cross-ensemble) SD calculated for the annual mean of each year separately. Fourth row: Change in the amplitude of snapshot SDs between the average over 1960-1989 and 2070-2099. Statistical significance of the changes (dots here reflect lack of significance $p \geq 0.05$) was determined based on the t -values of the two-sample Welch's t -test for the equality of temporal means of the ensemble standard deviations, with the equivalent sample sizes adjusted to account for serial correlations (see Methods). Note that for mean state changes, the absolute changes are shown, whereas for standard deviation

changes, relative changes are shown. Mean state changes in precipitation (e) is the same field shown in the central map in **Fig. 2**, but 2m reference temperature is used here whereas surface temperature is shown in **Fig. 2**.

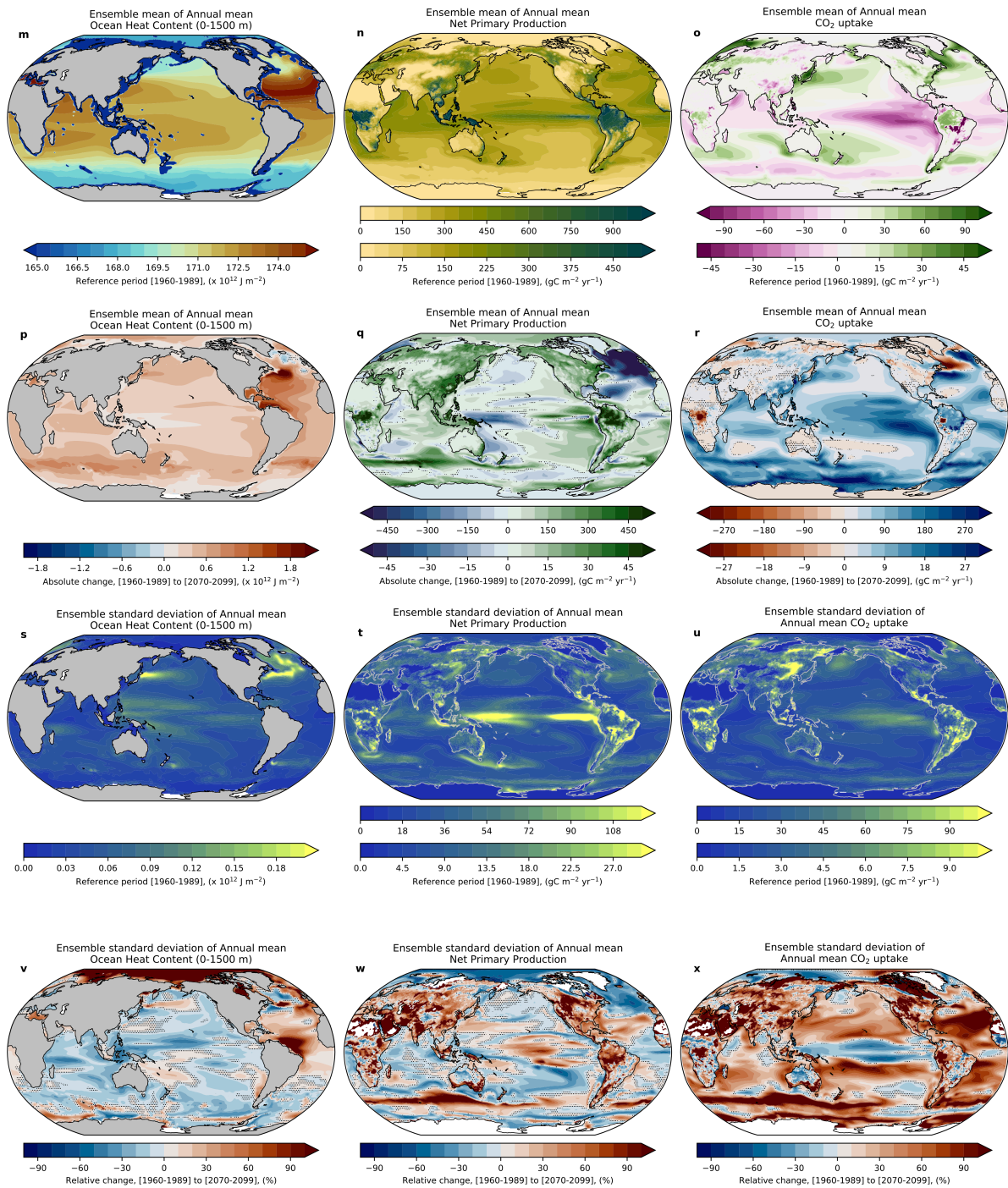


Fig. S4. (continued)

Patterns of change in CESM2-LE. First column: ocean heat content integrated over the upper 1500 m; Second column: net primary production (NPP); Third column: net CO₂ flux exchanged

with the atmosphere. First row: Mean state averaged over 1960-1989; Second Row: Change in mean state between 1960-1989 and 2070-2099; Third row: Average over 1960-1989 of snapshot (cross-ensemble) SD calculated for the annual mean of each year separately. Fourth row: Change in the amplitude of snapshot SDs between the average over 1960-1989 and 2070-2099. Statistical significance of the changes (dots here reflect lack of significance with $p \geq 0.05$) was determined based on the t -values of the two-sample Welch's t -test for the equality of temporal means of the ensemble standard deviations, with the equivalent sample sizes adjusted to account for serial correlations (see Methods). Note that for mean state changes, the absolute changes are shown, whereas for standard deviation changes, relative changes are shown. For each panel where two underlying colorbars are shown, the upper colorbar represents quantities over land and the lower colorbar represents quantities over the ocean.

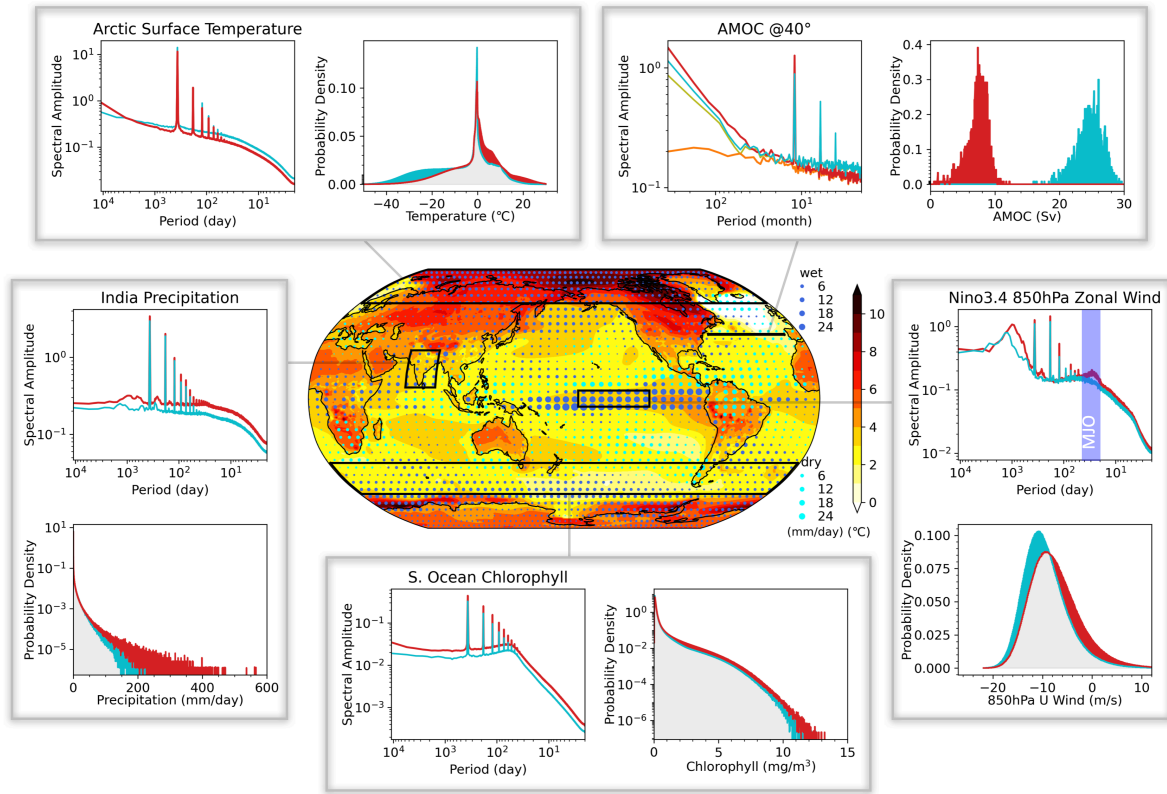


Fig. S5.

Changes in the Fourier amplitude spectrum of historical (1960-1989) to future (2070-2099) climate variability in CESM2-LE. The center map shows historical-to-future changes in surface temperature (shaded, °C) and precipitation (mm day⁻¹). Each pairing of panels shows this historical (cyan) and future (red) spectra and PDFs for five different variables over five different regions. Spectra are considered over the respective periods 1960-1989 (historical) and 2070-2099 (future), thereby including the trend, and PDFs are considered for all 365 days of 1989 and 2099 so as to minimize the impact of the trend. From upper-left clockwise, each pair of panels shows the historical (cyan) and future (red) of number of daily Arctic temperature (60°N-90°N), monthly Atlantic meridional overturning circulation (AMOC) at 40°N, daily zonal wind at 850 hPa over the Niño3.4 region (5°S-5°N, 170°W-120°W), daily surface chlorophyll concentrations over the Southern Ocean (60°S-40°S), and daily precipitation over India (7°N-30°N, 68°E-89°E). For AMOC variability, spectra of internal variability for the historical (olive) and future (orange) are also highlighted to show strong forced responses. The shaded area for the 850hPa zonal wind represents the Madden-Julian Oscillation (MJO) timescale. The Fourier spectra are calculated for timeseries at individual grid points including forced responses and internal variability and using 30-year intervals. Subsequently the spectra are averaged over the grid points in each region. PDFs of positive-definite variables (Southern Ocean surface chlorophyll and precipitation over India) are shown with logarithmic y-axes. Sharp spectral peaks are associated with the annual cycle and its non-sinusoidal components, which generate high order

harmonics. Spectra are shown as amplitude, with the units being the same as the x-axes for the PDFs. PDFs of positive-definite variables (S. Ocean chlorophyll and precipitation over India) are shown with logarithmic y-axes. The fields in the center panel are the same as those shown in **Fig. 2**.

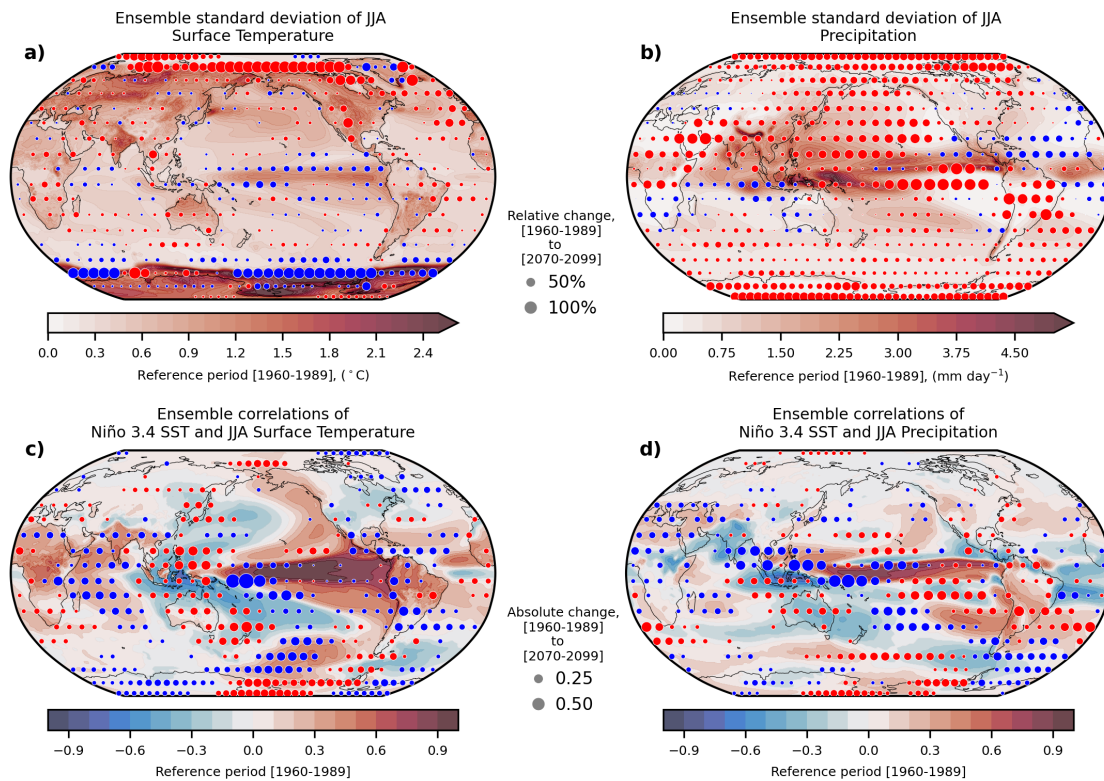


Fig. S6.

Changes in the patterns of interannual variability and correlation coefficients of June-July-August (JJA) season Niño3.4 index with surface temperature and precipitation. (Top) Colors show the time-averaged cross-ensemble standard deviation of the JJA seasonal mean surface temperature (a) and precipitation (b) for the period 1960-1989. Circles show the change in the stand deviations between 2070-2099 and 1960-1989, where insignificant change ($p \geq 0.05$) has been removed. (Bottom) Colors show ensemble-wise correlations of the Niño3.4 index with surface temperature (c) and precipitation (d) for JJA, averaged over the period 1960-1989. Circles show the change in correlations between 2070-2099 and 1960-1989, where statistically insignificant change ($p \geq 0.05$) has been removed. The Niño3.4 index for ENSO is the spatial average of sea surface temperature within 5°S - 5°N , 170°W - 120°W . Statistical significance of the changes (circles) was determined based on the p -values of two-sample Student's t -tests for the equality of temporal means of the ensemble standard deviations (top) and of the Fisher z -transformed correlation coefficients (3).

References

1. G. Danabasoglu, J. F. Lamarque, J. Bacmeister, D. A. Bailey, A. K. DuVivier, J. Edwards, L. K. Emmons, J. Fasullo, R. Garcia, A. Gettelman, C. Hannay, M. M. Holland, W. G. Large, P. H. Lauritzen, D. M. Lawrence, J. T. M. Lenaerts, K. Lindsay, W. H. Lipscomb, M. J. Mills, R. Neale, K. W. Oleson, B. Otto-Bliesner, A. S. Phillips, W. Sacks, S. Tilmes, L. van Kampenhout, M. Vertenstein, A. Bertini, J. Dennis, C. Deser, C. Fischer, B. Fox-Kemper, J. E. Kay, D. Kinnison, P. J. Kushner, V. E. Larson, M. C. Long, S. Mickelson, J. K. Moore, E. Nienhouse, L. Polvani, P. J. Rasch, W. G. Strand, The Community Earth System Model Version 2 (CESM2). *Journal of Advances in Modeling Earth Systems* **12**, 35 (2020).
2. M. J. E. van Marle, S. Kloster, B. I. Magi, J. R. Marlon, A. L. Daniau, R. D. Field, A. Arneth, M. Forrest, S. Hantson, N. M. Kehrwald, W. Knorr, G. Lasslop, F. Li, S. Mangeon, C. Yue, J. W. Kaiser, G. R. van der Werf, Historic global biomass burning emissions for CMIP6 (BB4CMIP) based on merging satellite observations with proxies and fire models (1750-2015). *Geoscientific Model Development* **10**, 3329-3357 (2017).
3. A. Timmermann, J. Sachs, O. E. Timm, Assessing divergent SST behavior during the last 21 ka derived from alkenones and G. ruber-Mg/Ca in the equatorial Pacific. *Paleoceanography* **29**, 680-696 (2014).